buildings

Article

Effects of Vertical Ground Motion on Pedestrian-Induced Vibrations of Footbridges: Numerical Analysis and Machine Learning-Based Prediction

Xinxin Wei [2], Bo Fu [1,*], Wenyan Wu [1] and Xinrui Liu [1]

[1] School of Civil Engineering, Chang'an University, Xi'an 710061, China
[2] Department of Civil and Environmental Engineering, Ruhr-Universität Bochum, Universitätsstraße 150, D-44780 Bochum, Germany
* Correspondence: 90_bofu@chd.edu.cn

Abstract: Current codes and guidelines for the dynamic design of footbridges often only specify the pedestrian-induced excitations. However, earthquakes may occur during the passing stage of pedestrians in earthquake-prone regions. In addition, modern footbridges tend to be slender and are sensitive to vertical ground motions. Therefore, we investigate the effects of vertical ground motion on pedestrian-induced vibrations of footbridges. A total of 138 footbridges with different materials, dimensions, and structural types are considered as the target structures. The classical social force model combined with the pedestrian-induced load is used to simulate crowd loads for the scenarios with six typical pedestrian densities. Furthermore, 59 vertical ground motions with four seismic intensities are taken as the seismic inputs. An amplification factor is introduced to quantify the amplification effects of vertical ground motion on human-induced vibrations of footbridges. Four machine learning (ML) algorithms are used to predict the amplification factor. The feature importance indicates that the scaled peak ground acceleration, the pedestrian density, and the bridge span are the three most important parameters influencing the amplification factor. Finally, the vibration serviceability of the footbridge subjected to both crowd load and vertical ground motion is assessed.

Keywords: footbridge; vibration; serviceability; crowd load; earthquake; machine learning

check for updates

Citation: Wei, X.; Fu, B.; Wu, W.; Liu, X. Effects of Vertical Ground Motion on Pedestrian-Induced Vibrations of Footbridges: Numerical Analysis and Machine Learning-Based Prediction. *Buildings* **2022**, *12*, 2138. https://doi.org/10.3390/buildings12122138

Academic Editor: Humberto Varum

Received: 26 October 2022
Accepted: 2 December 2022
Published: 5 December 2022

Publisher's Note: MDPI stays neutral with regard to jurisdictional claims in published maps and institutional affiliations.

Copyright: © 2022 by the authors. Licensee MDPI, Basel, Switzerland. This article is an open access article distributed under the terms and conditions of the Creative Commons Attribution (CC BY) license (https://creativecommons.org/licenses/by/4.0/).

1. Introduction

Pedestrians are the main users of footbridges. Therefore, pedestrian-induced footbridge vibration has drawn much attention from researchers in the past two decades, especially since the London Millennium Bridge incident that was induced by crowds [1]. Till now, researchers have made great contributions on human-induced loads [2–5], vibration serviceability evaluation [6–12], pedestrian–structure interaction [13–20], and pedestrian-induced vibration control [21–31]. The pedestrian-induced footbridge vibration falls into the serviceability category. Excessive vibration may cause pedestrian uncomfortableness and even endanger the bridge's safety. Correspondingly, several specifications have been issued, e.g., Sétra (2006) [32], ISO (2007) [33], and HiVoSS (2008) [34], regarding the serviceability design of footbridges. It is notable that current specifications for the dynamic design of footbridges only consider the relevant pedestrian-induced excitations.

When located in earthquake-prone regions, it is also possible that footbridges are subjected to not only pedestrian-induced loads but also ground motions. Simply, earthquakes can occur during the crowd passing process. In fact, the earthquake action is non-negligible for footbridges in earthquake-prone regions. In addition, modern footbridges tend to be slender, which makes these footbridges also sensitive to vertical earthquake loads. After the London Millennium Bridge incident, great efforts have been made to avoid lateral vibrations of footbridges. For instance, the UK National Annex to Eurocode 1 (2008) [35] specifies lock-in stability boundaries to avoid unstable lateral responses under crowd loads. However, vertical crowd-induced vibration is also an important issue and cannot be ignored. Therefore, this study mainly focuses on footbridge vibrations in the vertical direction, which is subjected to much larger loads than other directions. There are also studies investigating the influence of vertical ground motions on different types of structures, e.g., long-span cable-stayed bridges [36], segmental post-tensioned bridges [37], vehicle–bridge systems [38,39], long-span steel structures [40,41], long-span latticed arch-type structures [42], masonry structures [43], underground subway stations [44], undersea shield tunnels [45], and multi-directional base isolation systems [46]. The aforementioned studies indicate that vertical ground motion has a significant impact on structural performance. To the best knowledge of the authors, however, there is no existing research considering the combined effects caused by human-induced loads and vertical ground motions. It should be noted that the occurrence of an earthquake may induce crowd panic and increase the vibration. Therefore, it is quite meaningful to investigate the influence of vertical ground motion on crowd-induced vibration. Table 1 summarizes some representative references related to the topic of the current study.

To fill the gap, this study conducts a series of time-history analyses for 138 footbridges with various dimensions, materials, and structural types subjected to the combined actions of crowd-induced loads and vertical ground motions. The crowd-induced loads consider the crowd scenarios with six typical pedestrian densities ranging from 0.1 to 1.5 pedestrians/m^2. In total, there are 59 vertical ground motions with four different intensities for the seismic inputs. Thus, the total amount of calculation cases is 195,408 (=138 $\times$ 6 $\times$ 59 $\times$ 4). Furthermore, the amplification factor, which is defined as the ratio of the maximum acceleration induced by the combined actions to the maximum acceleration induced by crowds only, is calculated for each case and used as a guide for the serviceability design of footbridges subjected to both crowds and vertical ground motions. As there exists a strong nonlinear relationship between the inputs and the output (amplification factor), machine-learning (ML) techniques [47–52], which are quite suitable for solving nonlinear regression problems, are used to predict the amplification factor. Two individual-type ML algorithms, i.e., decision tree (DT) [53] and artificial neural network (ANN) [54], and two ensemble ML algorithms [55], i.e., random forest (RF) [56] and gradient boosting regression tree (GBRT) [51,52], are adopted to construct the predictive models. Ten parameters, including four structure-related parameters, pedestrians' density, and five earthquake-related parameters, are taken as the input variables, while the amplification factor is taken as the output variable. By using ML techniques, it relates the multiple factors (the structure, pedestrian, and earthquake parameters) to the amplification factor. Therefore, the total peak response of the structure due to combined loads can be obtained by multiplying the amplification factor with the pedestrian-induced vibration amplitudes. For a specific structure, the pedestrian-induced vibration levels can be conveniently measured by real-world measurements or predicted by numerical models. Finally, the vibration serviceability of the footbridge subjected to both crowd load and vertical ground motion is assessed.

The remaining parts of the paper are organized as follows. Section 2 introduces the simulation method and results of the footbridges under crowd loads. In Section 3, a total of 59 vertical ground motions with four intensities are selected. Section 4 investigates the influence of vertical ground motion on crowd-induced vibrations of footbridges. The amplification factor is then defined in Section 5. Four ML algorithms are adopted to predict the amplification factor based on a database containing 171,572 datasets. The vibration serviceability is evaluated in Section 6. Finally, several important conclusions are presented in Section 7.

Table 1. Summary of related previous research.

Reference Number	Authors (Year)	What Was Performed	Main Findings
1.	Pedestrian-induced loads and vibrations		
1.1	Human-induced loads		
[2]	Ingólfsson and Georgakis (2011)	A new stochastic load model was proposed to simulate the frequency and amplitude-dependent pedestrian-induced lateral forces.	The prediction of the critical number of pedestrians is consistent with the incident on the London Millennium Bridge.
[3]	Racic and Brownjohn (2012)	A mathematical model was developed to create synthetic narrow-band lateral forces induced by pedestrians.	The model can be used to assess the dynamic performance in everyday design practice.
[4]	Bruno and Corbetta (2017)	A new multi-scale model was developed to simulate uncertainties in pedestrian traffic.	The variability of traffic random variables is larger than structural properties ones.
[5]	Casciati et al. (2017)	A time-variant stochastic field model was proposed to model the walking forces induced by a small group of pedestrians.	The developed model can consider different idealizations of human-induced excitation and can be used in a serviceability limit state design.
1.2	Vibration serviceability evaluation		
[6]	Bruno and Venuti (2010)	A simplified serviceability assessment method for footbridges under lateral crowd loading was proposed.	The proposed method can reflect the actual walking behaviour of pedestrians by using the speed–density and frequency–speed relationship.
[7]	Živanović (2012)	A comprehensive experimental dataset of a box-girder footbridge that is lively in the vertical direction was provided.	Walking frequency, step length, and pedestrian speed in normal traffic obey a normal distribution, while pedestrian arrival time follows a Poisson distribution.
[8]	Setareh (2016)	Three important issues regarding vibration serviceability were investigated on a slender steel footbridge.	When the crowd speed closes to the first-mode resonance frequency of the footbridge, the enhancement factor for the group effect becomes closer to the group size.
[9]	Bedon (2019)	A preliminary dynamic characterization of an existing suspension glass footbridge was presented using on-site vibration tests and refined Finite Element methods.	A combination of multiple aspects has a significant influence on the structural performances and modal dynamic estimations.
[10]	Feng et al. (2019)	The acceleration of 21 pedestrian bridges in Beijing were recorded under different service conditions.	The fundamental frequency and acceleration are the two most important controlling factors in vibration serviceability design.
[11]	Fu and Wei (2021)	A two-stage ML-based analysis method for the human-induced vibration of a concrete footbridge was proposed.	The elastic modulus of concrete can markedly affect the human-induced vibration of concrete footbridges
[12]	Gong et al. (2022)	The vibration serviceability of two recent long-span footbridges in China was comprehensively assessed with six current specifications.	The total structural responses considering the contributions of closely spaced multiple modes are significantly larger than those using the specifications based on the single dominating mode only.

Table 1. *Cont.*

Reference Number	Authors (Year)	What Was Performed	Main Findings
1.3 Pedestrian–structure interaction			
[13]	Morbiato et al. (2011)	The pedestrian–structure interaction was considered by developing a non-linear double pendulum model.	When synchronization occurs, pedestrian motion becomes in-phase quadrature with a quarter-of-period before the bridge motion.
[14]	Carroll et al. (2012)	A discrete element theory (DET)-based method was proposed to simulate the crowd–bridge interaction.	The proposed method can predict emergent crowd behaviour better than earlier hydrodynamic models.
[15]	Jiménez-Alonso et al. (2016)	A biomechanical crowd–structure interaction model was developed.	The proposed model can accurately reflect the change in the dynamic properties of the structure induced by pedestrian flows.
[16]	Shahabpoor et al. (2017)	A vibration serviceability assessment method was proposed according to the actual vibration level experienced by each pedestrian.	The method can accurately estimate the structural responses compared to current design guidelines.
[17]	Toso et al. (2017)	A fully synchronized force model for walking pedestrians was proposed and compared with a simple force-only model and experimental vibration data was recorded in a real composite footbridge.	The proposed model can improve the simple force-only model and this may obtain a more realistic simulation of the dynamic structural behaviour.
[18]	Mulas et al. (2018)	The footbridge-walking pedestrian coupled equation of motion in the vertical direction was analytically derived using Lagrange's equation and a discrete modelling framework.	The numerical simulations exhibit significant variability in the response due to relatively small variations in the loading scenarios.
[19]	Setareh and Gan (2018)	The human–structure interaction on the dynamic behaviour of a slender two-span steel footbridge was studied.	The contribution of the wood decking to the structural stiffness is limited while their mass can be included.
[20]	Ahmadi et al. (2019)	The influence of human–structure interaction on the structural response of a lively lightweight GFRP footbridge was studied.	The bridge vibration has a significant impact on walking force, and to a lesser extent on the dynamics of the human–structure system.
1.4 Pedestrian-induced vibration control			
[22]	Li et al. (2010)	The multiple tuned mass damper (MTMD) designed by a random optimization procedure was adopted to reduce the crowd-induced vibration of a footbridge.	The proposed MTMD is more effective than the traditional MTMD in terms of reduction efficiency and reducing the off-tuning effect of MTMD.
[24]	Venuti and Bruno (2013)	A new strategy of using walkway shaping was developed to mitigate the human-induced lateral vibrations on footbridges.	The new strategy is less expensive and more durable than traditional structural countermeasures based on increasing stiffness and damping, respectively.
[27]	Venuti and Anna (2018)	A crowd flow control strategy by installing obstacles located along the footbridge span was proposed to control the human-induced vertical vibrations of footbridges.	The maximum reduction of 31% can be achieved if the obstacles are placed to generate local bottlenecks along the footbridge.
[31]	Gong et al. (2021)	The effectiveness of installing TMD on mitigating the pedestrian-induced vibration on a typical glass suspension footbridge in China was studied.	The commonly used TMD can effectively reduce the vibration levels of the footbridge.

Table 1. *Cont.*

Reference Number	Authors (Year)	What Was Performed	Main Findings
2.	Seismic performance of long-span structures subjected to vertical earthquakes		
[36]	Shrestha (2015)	The effect of the near-fault vertical ground motions on the seismic response of a long-span cable-stayed bridge was numerically studied.	Vertical displacement of the bridge deck at mid-span is sensitive to vertical ground motion.
[40]	Xiang et al. (2017)	The seismic response of steel structures subjected to vertical seismic excitation was studied by using an idealized model and inelastic displacement ratio.	The inelastic displacement ratio-based method can estimate the seismic responses of steel structures subjected to severe vertical ground motions.
[41]	Fayaz and Zareian (2019)	The influences of the vertical component of near-fault ground motions on special moment-resisting steel frames and special concentrically braced frame-braced steel frames were studied.	The current seismic load combinations in ASCE 7 are inadequate to consider the influences of the vertical near-fault ground motions.
[42]	Qu et al. (2019)	An improved multidimensional modal pushover approach with two-stage analyses was developed for seismic assessment of latticed arches subjected to lateral and vertical ground motions.	The developed method has good agreement with those of time-history analysis and is superior to the existing methods in terms of accuracy.

The main contributions of the study can be summarized as three aspects. Firstly, the structural responses of footbridges subjected to the combination of crowd loads and vertical earthquakes are analysed. Secondly, a huge amount of time-history analysis is conducted to consider the influences of structure-related, crowd-related, and earthquake-related parameters on the structural responses. Thirdly, four ML models are used to predict the amplification factor.

The driving ideas traced from the literature review and organization of the paper are depicted in Figure 1.

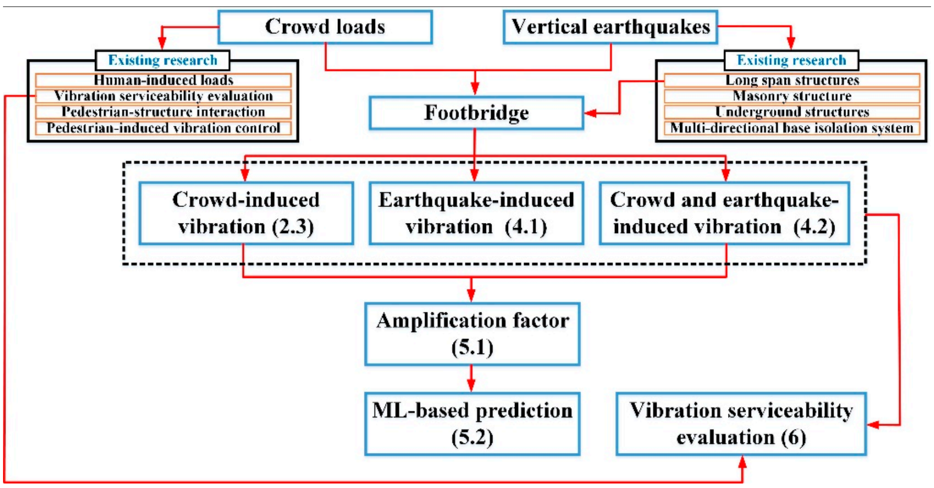

Figure 1. Driving ideas traced from the literature review and organization of the paper.

2. Simulation of Footbridge Vibration under Crowd Loads

2.1. Analytical Model of Footbridge

Wei et al. (2019) [57] comprehensively reviewed 138 footbridges, which were mostly built after 1991 and reported in the literature, e.g., 73 footbridges were also evaluated by [58]. In this study, an analytical footbridge model is constructed based on the typical characteristics of real-world footbridges as summarized by Wei et al. (2019) [57] and the popular guidelines, e.g., Sétra and HiVoSS. Typical footbridge characteristics are summarized as follows.

- Material: Different materials are applied in footbridge construction. As shown in Figure 2a, conventional construction materials include steel, concrete, steel–concrete composites, timber, and aluminium. Almost half of the footbridges are made of steel (67/138, i.e., 48.6%). Furthermore, the proportion of concrete footbridges is over a quarter (38/138, i.e., 27.5%). New constructional materials such as FRP (14/138, i.e., 10.1%) are also increasingly applied. Based on available data, the conventional footbridges (1200 kg/m^2) can be approximately 8.6 times heavier than FRP footbridges (140 kg/m^2), in terms of the physical mass per square meter.
- Dimension: Very few bridge decks have variant widths along the spans, with almost all bridge decks being typical rectangles. The rectangular decks vary in the main spans and widths of bridge decks (Figure 3a). For those bridges with variable widths along the spans, the corresponding mean widths are considered in Figure 3a. As presented in Figure 3a, the spans and widths are within the ranges of [4.8, 230] m and [0.78, 13.4] m, respectively. In particular, most spans and widths are correspondingly smaller than 50 m and 5 m, respectively. Furthermore, no obvious trend is found between the width–span relationships.
- Structural type: To satisfy engineering and realistic needs, different types are selected in bridge construction (Figure 2b). Most footbridges are typical bridge types, e.g., girder (25.4%), truss/truss-girder (20.3%), arch (10.9%), cable-stayed (9.4%), suspension (5.1%), and stress-ribbon (2.9%). The remaining bridge types are unknown due to unavailable information from the literature [57,58]. The boundary conditions of the reported footbridges are basically simply supported. Simply supported is not only the simplest boundary condition, but also the basic element for other more complex boundary conditions [59]. This is also in accordance with the common practice that, in the calculations of human-induced vibrations for footbridges, it often applies a simply supported beam model with sinusoidal mode shapes as the analytical model [60–63]; when experimental data with good quality are available, a good match between the calculated and measured responses can often be obtained, e.g., with the help of model updating techniques [64].
- Fundamental natural frequency: Figure 3b shows the fundamental natural frequencies of the vertical modes for the bridges. Most of the frequencies are below 5 Hz and may fall into the frequency range of human-induced excitations [32,34]. Furthermore, the fundamental natural frequency $f_{1,v}$ (unit: Hz) basically follows a fitted numerical relationship with the main span L (unit: m) as [57]:

$$f_{1,v} = \frac{100.5}{L} \tag{1}$$

- Damping ratio: The damping ratios fall within the range of [0.14%, 7.9%]. Based on the estimated non-exceedance probability, less than 50% of the footbridges have damping ratios higher than 1.0%. Most (92%) damping ratios are lower than 3%.

To model real-world footbridges as realistically and simply as possible, an analytical model is proposed. The model considers different construction materials, bridge span lengths and widths, natural frequencies, damping ratios, modal masses, etc. Different boundary conditions and cross-sectional properties can also be considered when necessary.

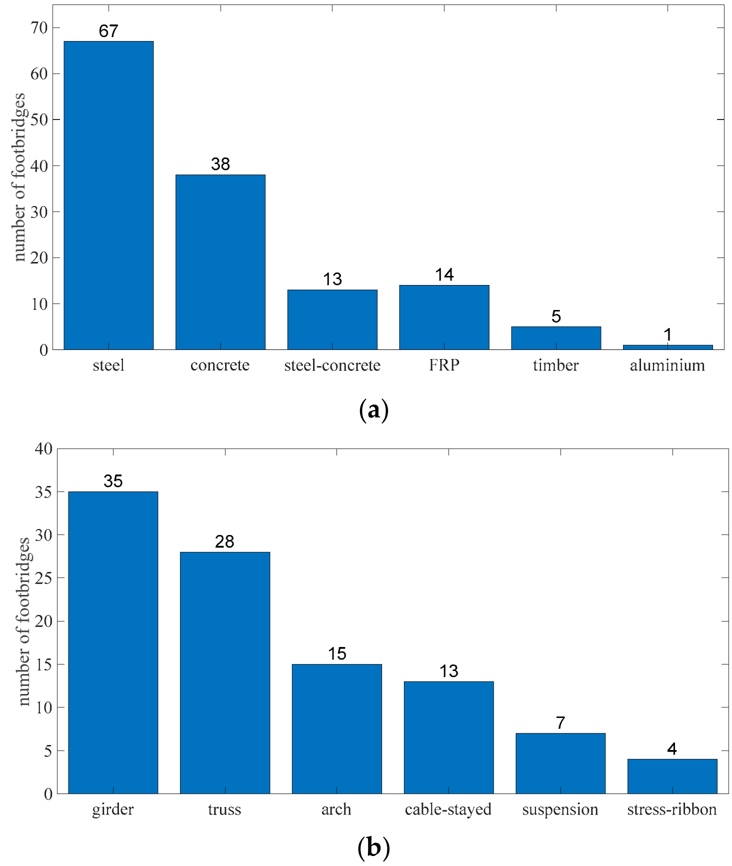

Figure 2. Number of footbridges. (**a**) Construction materials; (**b**) bridge types.

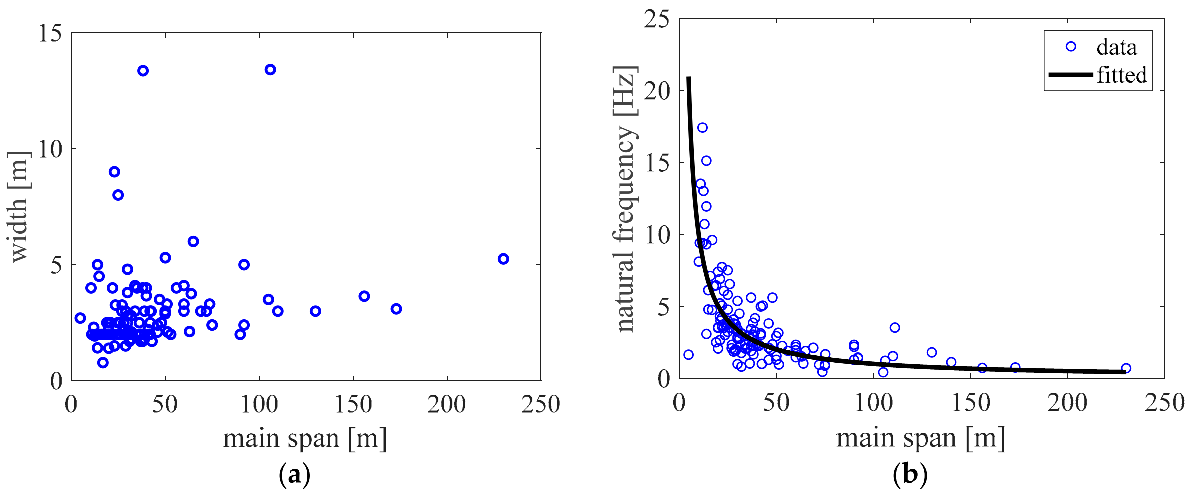

Figure 3. Plots of (**a**) main widths and (**b**) fundamental natural frequencies of the vertical modes over the main spans of constructed footbridges.

Therefore, in the current investigations, the basic assumptions of the proposed analytical model are:

1. Bridge type, boundary conditions, and mode shapes: The simply supported beam-like footbridge with sinusoidal mode shapes is considered as the basic analytical model [65]. The applied analytical model of the footbridge is idealized as a simply supported beam in the vertical (Z) direction. The bridge deck has a rectangular walking surface in the XY plane, with X the longitudinal direction and Y the lateral direction.

2. Bridge deck span lengths and widths: The considered bridge decks are typical rectangles with different widths and lengths as summarized by the real-world footbridges in Figure 3.
3. Natural frequencies, damping ratios, and modal masses: The fundamental natural frequencies, as shown in Figure 4, are calculated based on the span length, according to Equation (1). In Figure 4, the solid line is the mean value of the frequencies, while the two dashed lines represent mean $\pm$ St.D. (standard deviation). The damping ratios are random values within the range of [0.14%, 7.9%]. However, in this study, damping ratios are assumed to be identical if the bridge is made of the same material. Typical (average) damping ratios for different materials are 0.4% (steel), 1.3% (concrete), 0.6% (steel–concrete), 1.5% (timber), 1.1% (aluminium), and 2.5% (FRP), according to the real-world footbridges [57] and HiVoSS guidelines. Therefore, the aforementioned six damping ratios are used in the following analytical analysis. The modal masses of the fundamental mode can be set as half of the total masses of the footbridges, which are mainly governed by the construction material density, cross-sectional properties, and bridge length and width. In accordance with the ratio of the physical mass per square meter [57] for conventional and FRP footbridges, the modal masses of conventional footbridges are considered as 8.6 times higher than FRP footbridges. Specially, the modal mass for the fundamental vertical mode is considered as:

$$M_{1,v} = \frac{m \cdot L \cdot W}{2} \tag{2}$$

with m the physical mass per square meter, i.e., $m = 1200\ \mathrm{kg/m^2}$ for conventional footbridges and 140 $\mathrm{kg/m^2}$ for FRP footbridges [57], while W is the bridge width.

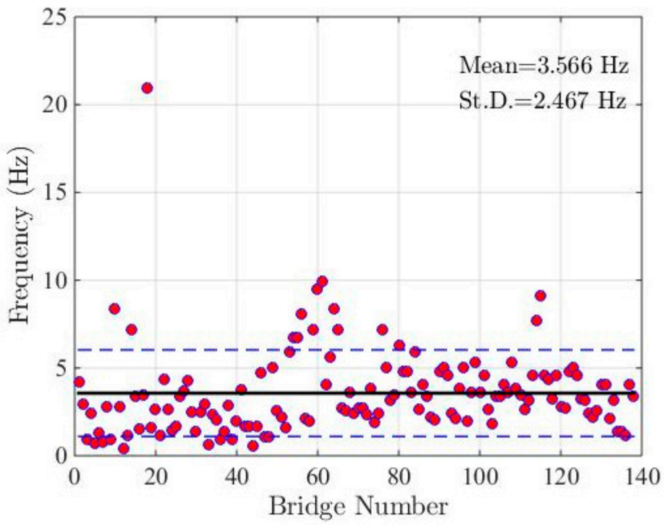

Figure 4. Natural frequencies of the first bending mode for the analytical structures.

According to modal analysis of the simply supported beam [65], the mode shape, natural frequency, and modal mass of the nth vertical mode are expressed as Equations (3)–(5), respectively. It should be noted that the current study assumes that the structure has constant natural frequencies and damping ratios. In the future study, it is more realistic to use variable natural frequencies and damping ratios induced by long-term effects such as prestressing losses [66–68].

$$\varnothing_{n,v}(x) = \sin\left(\frac{n\pi x}{L}\right) \tag{3}$$

$$f_{n,v} = n^2 \cdot f_{1,v} = n^2 \cdot \frac{100.5}{L} \tag{4}$$

$$M_{n,v} = M_{1,v} = \frac{m \cdot L \cdot W}{2} \tag{5}$$

2.2. Model of Crowd-Induced Loads under Evacuation

2.2.1. Crowd-Induced Load

During the crowd evacuation on a footbridge, each person excites the structure. The human-induced load of a person in a crowd is not the same as the case when he/she is in free walking status. In particular, his/her behaviour is affected by others and the surroundings [61,62,69]. Thus, it is realistic to consider the inter- and intra-subject variabilities in pedestrian behaviour and the induced forces. To model the pedestrian evacuation behaviour, a microscopic crowd evacuation model is required.

Since its development in 1995 [69], the social force model has been widely applied to simulate pedestrian dynamics in many applications, such as in transport stations, buildings, and other urban public area scenarios [70]. Despite its simplicity of mathematical formulation, the model demonstrates a good ability of pedestrian dynamics reproduction. Till now, the model has been applied not only for crowd evacuation in normal situations [69], but also for unusual situations when people are in panic mode [71], e.g., in earthquakes [72]. Thus, in this study, the social force model is utilized to model the crowd evacuation behaviour during an earthquake. The crowd's evacuation behaviour is guided by physical and psychological interactions with other persons and borders (obstacles). These physical and psychological interactions are considered as physical and psychological forces (accelerations), respectively. Based on Newtonian mechanics, for a random pedestrian α with a mass of m_α, the relationship between displacements (time-variant location $\vec{r}_\alpha(t)$), velocities (time-variant velocity $\vec{v}_\alpha(t)$), and accelerations (time-variant acceleration $\vec{a}_\alpha(t)$) are coupled as:

$$\frac{\mathrm{d}\vec{r}_\alpha(t)}{\mathrm{d}t} = \vec{v}_\alpha(t) \tag{6}$$

$$\frac{\mathrm{d}\vec{v}_\alpha(t)}{\mathrm{d}t} = \vec{a}_\alpha(t) = \frac{\vec{F}_\alpha(t)}{m_\alpha} \tag{7}$$

The solutions of these coupled equations output the real-time walking behaviour, i.e., the realistic evacuation behaviour of each person in earthquakes. By including pedestrian-induced forces following the time-variant pedestrian locations and velocities, the crowd-induced loads under an evacuation scenario are obtained. The harmonic load model in terms of Fourier series from Bachmann and Ammann (1987) [73] was applied. To be concise, detailed information on crowd behaviour modelling and crowd-induced load formulation is referred to in [11,61,62,69,71].

2.2.2. Parameter Settings

This subsection presents the parametric settings for a case of the structure with main span length L = 50 m and width W = 3 m. Table 2 summarizes the six representative crowds with different pedestrian densities ρ_{crowd}, from 0.1 (very weak traffic) to 1.5 (exceptionally dense traffic) pedestrians/m^2, as defined in HiVoSS.

Table 2. Parameters of considered crowds.

Pedestrian Density (Pedestrians/m^2)	Number of Persons (-)	Arrival Time of First Person (s)	Arrival Time of Last Person (s)	Expected Speed (m/s)	Expected Passing Time (s)
0.1	15	3.56	34.86	1.34	37.32
0.2	30	3.32	37.32	1.34	37.32
0.5	75	2.26	35.96	1.30	38.50
0.8	120	0.80	42.90	1.17	42.90
1.0	150	0.38	46.96	1.06	47.26
1.5	225	0.22	61.74	0.81	61.99

For each simulated scenario, it assumes that when people are evacuating on the bridge from one end ($x = 0$) to another end ($x = L$), the earthquake occurs at a random time instant t_{eq}. The arrival times on the bridge of the pedestrians are assumed to follow a Poisson distribution [7,61]. The arrival times of the first and last persons are listed in Table 2. For instance, for 0.1 pedestrians/m^2, the first pedestrian arrives on the structure at a time instant $t_1 = 3.56$ s. The arrival time of the last person is $t_{25} = 34.86$ s, where the subscript 25 denotes the number of pedestrians for 0.1 pedestrians/m^2. For 1.5 pedestrians/m^2, the first pedestrian arrives on the structure at a time instant $t_1 = 0.22$ s. The arrival time of the last person is $t_{375} = 61.74$ s, where the subscript 375 denotes the number of pedestrians for 1.5 pedestrians/m^2. The pedestrians arrive on the bridge with random positions, i.e., with a random value of a coordinate in the Y direction in the range of $[r_\alpha, W - r_\alpha]$. r_α is the radius of a random pedestrian α and thus the range meets the minimum requirement of the pedestrian body to avoid a collision with the borders. As suggested by [61,63], r_α is assigned as 0.3 m.

The initial desired speeds of the crowd can be described as following a normal distribution: $N(1.34,\ 0.26)$ m/s [69]. In a pedestrian crowd in daily-life conditions, the mean walking speed decreases with an increase in crowd density, according to experimental observations by [74]. Detailed formulations on the relationship between the speed of movement and crowd density is referred to in [75]. Based on their results, the expected mean walking speeds and average passing times of the crowd are determined for walking crowds in normal situations. For example, as shown in Table 2, mean walking speed is expected to be approximately 1.34 m/s and 0.81 m/s for densities of 0.1 and 1.5 pedestrians/m^2, respectively. Correspondingly, it can be predicted that the crowd needs approximately 37.32 s and 61.99 s to pass the bridge, respectively. Due to a lack of real-world walking speed data of pedestrian evacuation in earthquakes, the average passing times needed in normal situations for each relevant density case are considered as the time span in the simulations. The time steps in the crowd simulations are adopted as 0.02 s, in accordance with the time step of the recorded earthquake accelerations.

For any other footbridges with different main span lengths and widths, similar procedures can be taken as the illustrative example. For different span lengths and widths, the corresponding arrival times of pedestrians may be different.

2.3. Dynamic Response of Bridge under Crowd Loads

In this subsection, the structural responses due to crowd loads are calculated. The social force model with the parametric values used in the illustrative example is applied to realistically simulate crowd behaviour. The induced vibrations by the pedestrian crowd are also determined.

2.3.1. Simulated Crowd Behaviour

Figure 5 shows the mean speed of the dynamic crowd on the bridge. For both densities, in the first approximately 5 s, the mean walking speed experiences abrupt changes. This results from the fact that it needs large adjustments in walking parameters at the entrance of the bridge, where newly arrived persons start evacuations and need more sufficient adjustments (see Figure 5). For most of the time instants after the initial stage, the mean speed of the crowd fluctuates at a lower value than the desired mean speed. This demonstrates that after the initial stage, walking speeds are partially restricted in the crowd. Late-arriving persons tend to maintain similar walking speeds as the pedestrians ahead. These ‘traffic jam’ effects most probably occur in a very crowded situation. After the fluctuation stage, the mean walking speed in a high pedestrian density crowd decreases gradually with increasing pedestrian numbers on the bridge. For the low-density case, the mean speed can even show an increasing trend after the abrupt fluctuation stage, depending on the initial desired walking speed of the persons. This reflects the fact that ‘conflicts’ among pedestrians do not occur very often in a low-density crowd. Thus, late-arriving faster pedestrians can maintain their walking speeds for a longer time. Furthermore, the mean speed in the low-density case is more sensitive to the scatter in the initial desired walking speeds of newly arrived pedestrians in the crowd. It also proves that the speed–density relationship in earthquakes may be quite different from the experimental observations from daily-life conditions as discussed in [74]. The pedestrian evacuation in earthquakes may suffer from anxiety and even panic. The walking speeds in earthquakes may experience more abrupt changes.

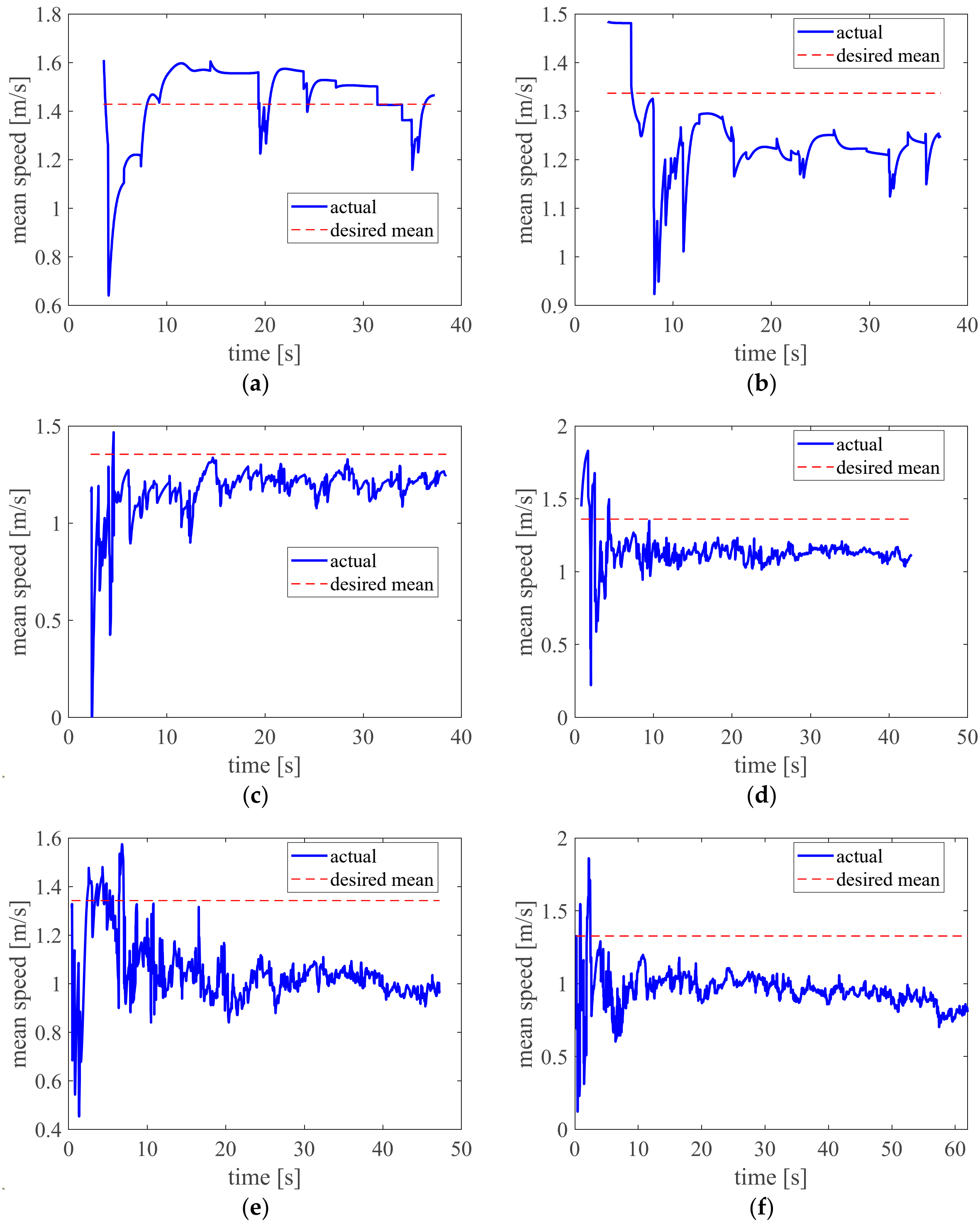

Figure 5. The mean speed of real-time evacuating persons on the bridge. (**a**) 0.1 pedestrians/m^2, (**b**) 0.2 pedestrians/m^2, (**c**) 0.5 pedestrians/m^2, (**d**) 0.8 pedestrians/m^2, (**e**) 1.0 pedestrians/m^2, (**f**) 1.5 pedestrians/m^2.

Figure 6 presents the behaviour of an evacuating pedestrian in a crowd who arrives on the bridge at 4.14 s and stops walking at 37.32 s when the simulation ends. As shown in Figure 5, more abrupt changes in the walking speed are observed during the first approximately 5 s, when the person needs to quickly adjust his/her walking parameters when entering the bridge to avoid collisions as much as possible.

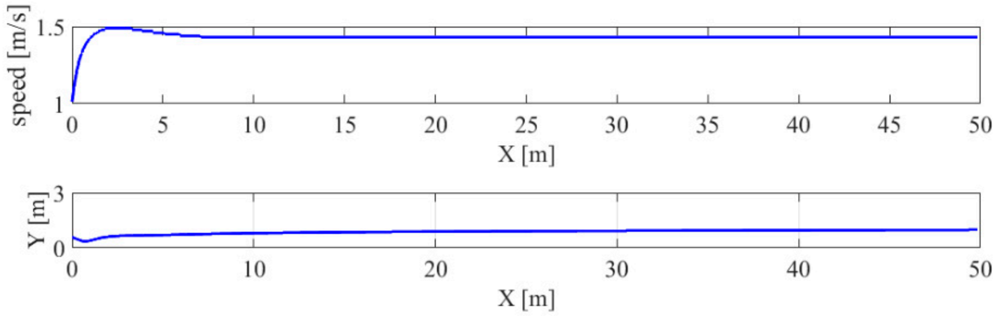

Figure 6. The walking speed (figure above) and trajectory (figure below) of a random pedestrian who arrives at 4.14 s and stops walking at 37.32 s when the simulation ends.

2.3.2. Single Pedestrian-Induced Forces and Vibrations

Figure 7 illustrates the representative person-induced walking forces in the vertical (Z) direction acting on the structure. The excited walking forces are not perfectly harmonic loads because the step frequencies are time-variant, resulting from the time-variant walking speeds. The most 'imperfect' part is at the beginning when the person arrives on the structure, which is in accordance with abrupt changes in both the walking speed and trajectory, as shown in Figure 6.

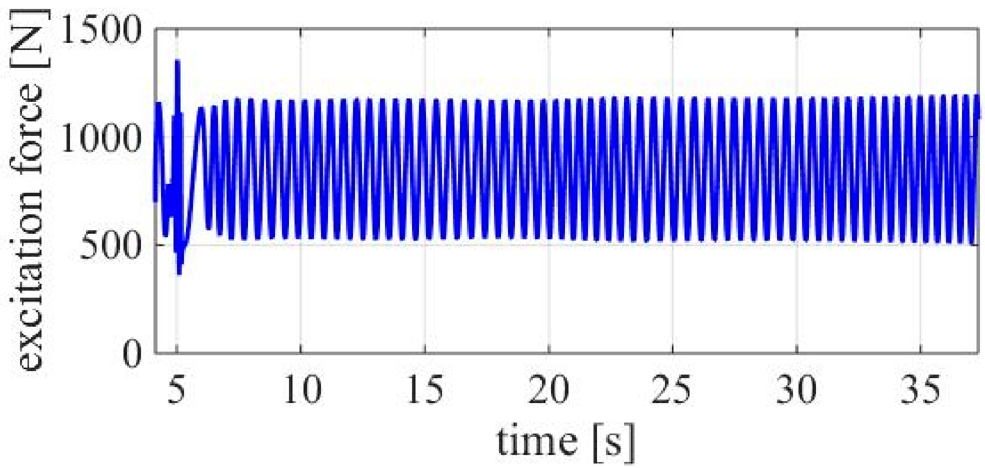

Figure 7. The time history of a representative single pedestrian-induced load in the vertical (Z) direction. The pedestrian is the one who arrives at 4.14 s and stops walking at 37.32 s when the simulation ends.

Figure 8 shows the real-time induced structural responses in the vertical (Z) direction by the representative person. The amplitude of the vertical responses is 0.08 m/s^2. The maximum acceleration amplitudes occur when the person is passing near the midspan of the structure, as the time instant when the modal load amplitudes are a maximum.

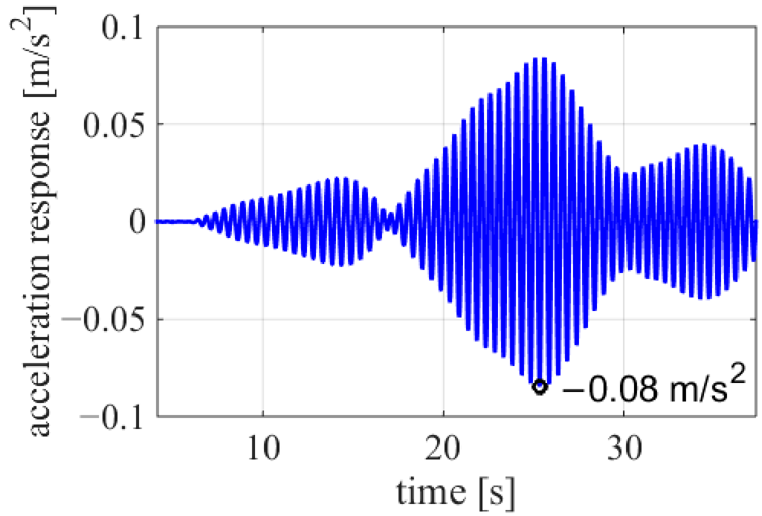

Figure 8. The time history of a representative single pedestrian-induced vibrations in the vertical (Z) direction at the midspan of the structure. The pedestrian is the one who arrives at 4.14 s and stops walking at 37.32 s when the simulation ends.

2.3.3. Crowd-Induced Loads and Vibrations

The crowd-induced loads are obtained by superimposing the force contributions of all individuals, who have different timings for arriving and leaving the bridge. For each time instant, it considers all the real-time persons on the bridge. Figure 9 depicts the time-variant crowd-induced loads in the vertical (Z) direction for different pedestrian densities. As expected, the load fluctuates and has a general increasing tendency with time due to the increasing number of pedestrians for each density case. The fluctuations in the induced load are caused by the adjustments of walking parameters of pedestrians in the crowd. The minimum and maximum load are induced by the lowest and the highest considered density of 0.1 and 1.5 pedestrians/m^2, respectively. Furthermore, the load increases nonlinearly with the density. It results from the crowd-induced load being superimposed by the force contributions of all single persons, while each pedestrian has different timings for arriving and leaving the bridge and different timings for each footfall.

Figure 10 exhibits the time history of the crowd-induced vibrations in the vertical (Z) direction for different pedestrian densities. The lowest and highest structural responses are obtained for the lowest and highest density of 0.1 and 1.5 pedestrians/m^2, respectively. The maximum acceleration response amplitude does not always increase with the density, with the turning point at a density of 0.8 pedestrians/m^2. At the case with 0.8 pedestrians/m^2, although the crowd-induced loads are higher than the lower density cases, the corresponding excitation frequency contents are off the near-resonance.

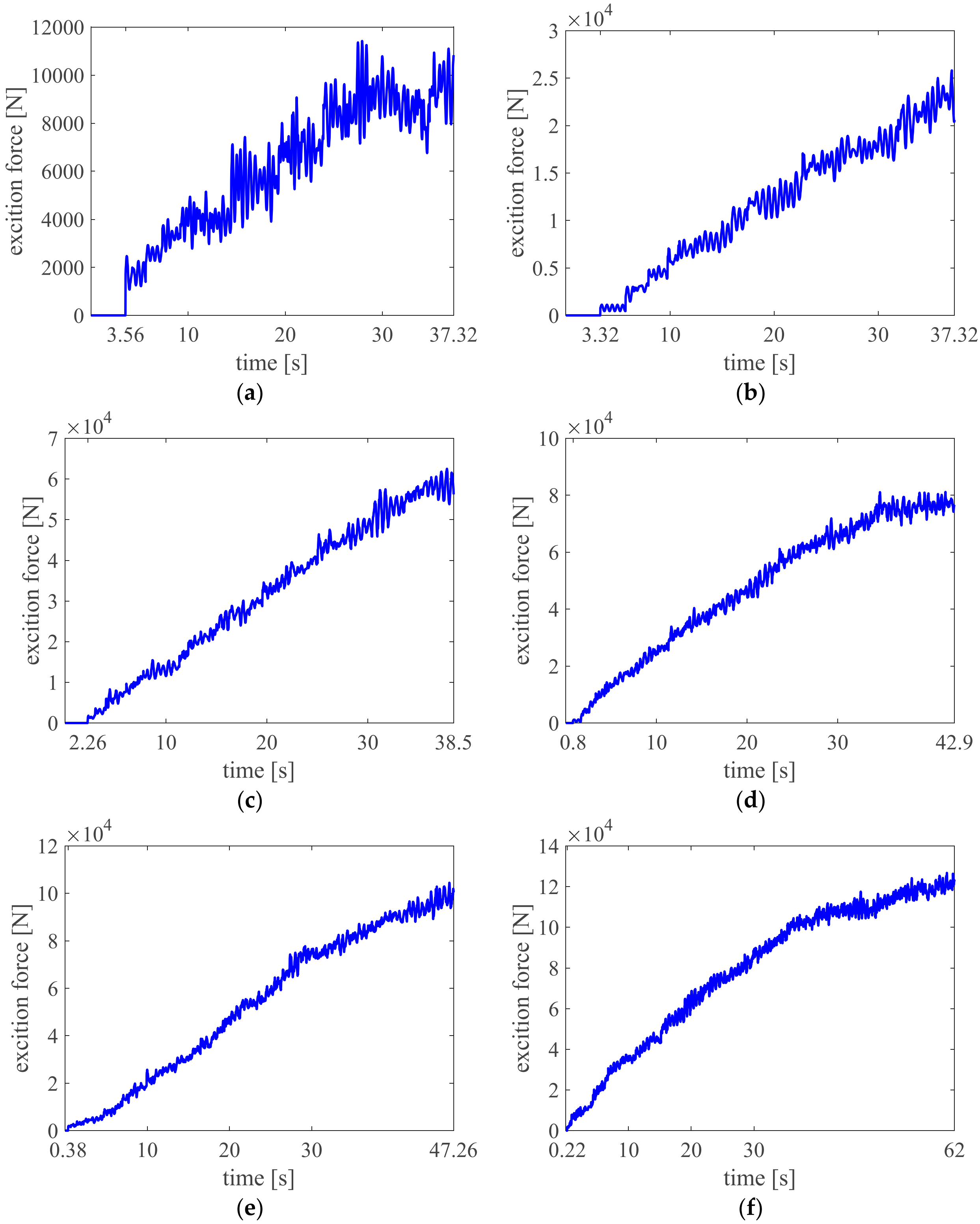

Figure 9. The time history of the crowd-induced loads in the vertical (Z) direction for different pedestrian densities. (**a**) 0.1 pedestrians/m^2, (**b**) 0.2 pedestrians/m^2, (**c**) 0.5 pedestrians/m^2, (**d**) 0.8 pedestrians/m^2, (**e**) 1.0 pedestrians/m^2, (**f**) 1.5 pedestrians/m^2.

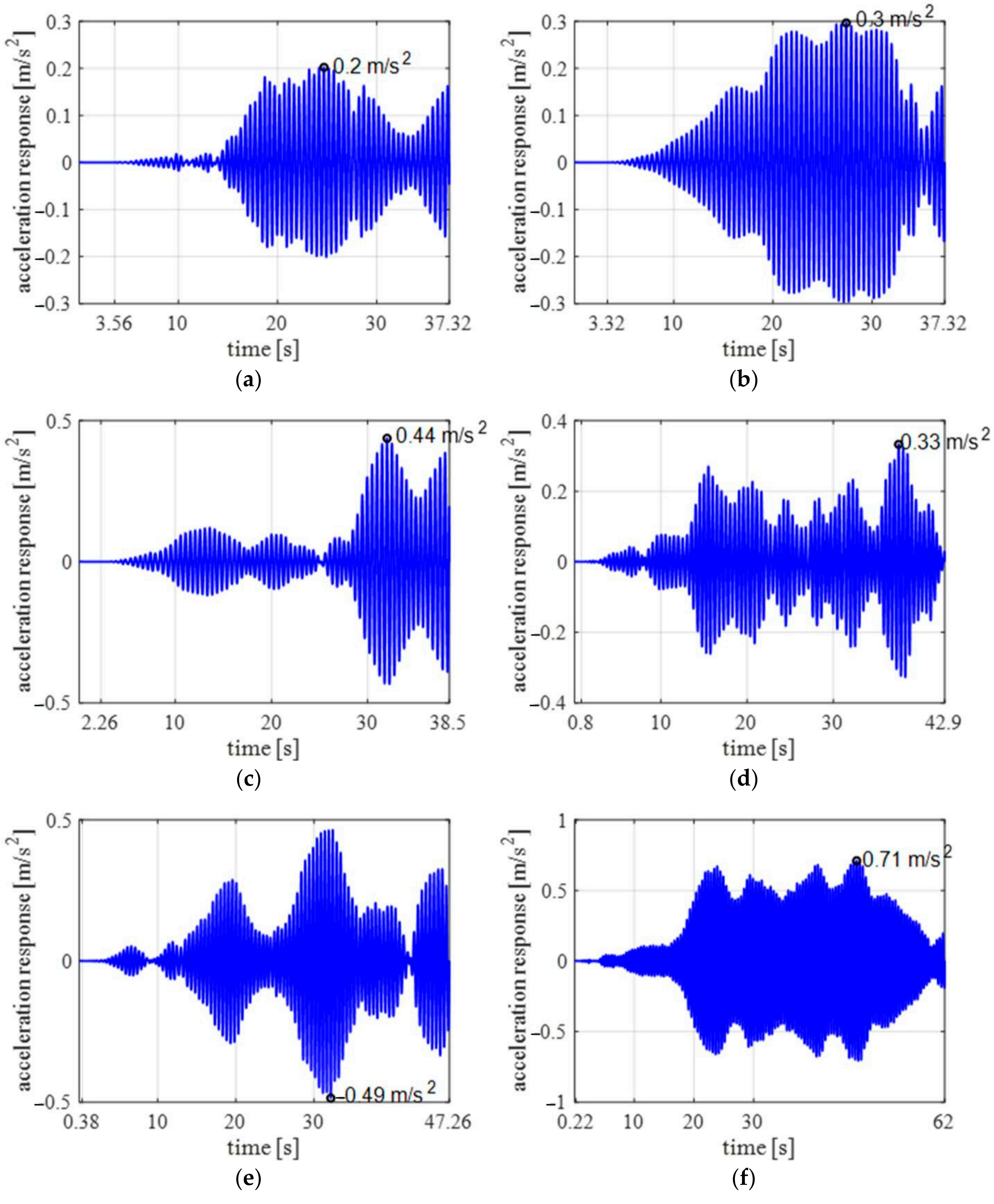

Figure 10. The time history of crowd-induced vibrations at the midspan of the structure in the vertical (Z) direction for different pedestrian densities. (**a**) 0.1 pedestrians/m^2, (**b**) 0.2 pedestrians/m^2, (**c**) 0.5 pedestrians/m^2, (**d**) 0.8 pedestrians/m^2, (**e**) 1.0 pedestrians/m^2, (**f**) 1.5 pedestrians/m^2.

3. Vertical Ground Motions

In this study, a total of 59 vertical earthquake records are collected from a publicly accessible database via the website (https://www.strongmotion.org/, accessed on 6 February 2021). The original peak ground accelerations (PGAs) of the 59 earthquake records range from 0.054 g to 2.370 g. Apart from PGA, three other intensity measures, i.e., peak ground velocity (PGV), $S_{a\text{-}1s}$ (spectral acceleration at a period of 1 s), and $S_{a\text{-}2s}$ (spectral acceleration at a period of 2 s), are also taken to characterize the ground motions. The basic information of the selected vertical ground motions is summarized in Table 3. It is assumed that the bridge is located in regions in China with seismic intensities of 6, 7, 8, and 9 [76]. When conducting elastic time-history analysis of the horizontal earthquakes, the PGAs of the minor earthquakes with a return period of 50 years should be scaled to 0.018 g, 0.035 g, 0.07 g, and 0.14 g for the four intensities, respectively. Furthermore, it is recommended that the V/H (Vertical to Horizontal) ratio should be large or equal to 2/3 (e.g., [44]). Finally, the PGAs of the selected vertical ground motions are scaled to 0.012 g, 0.023 g, 0.047 g, and 0.093 g for the four intensities, respectively. Figure 11 shows the response spectra and average spectrum of the scaled vertical ground motions.

Table 3. Vertical ground motions used in this study.

Number	Earthquake	Station	Year	Magnitude	PGA (g)	PGV (m/s)	$S_{a\text{-}1s}$ (g)	$S_{a\text{-}2s}$ (g)
1	Gazli, Uzbekistan	Karakyr	1976	6.8	1.257	0.602	0.515	0.153
2	Kobe, Japan	Nishi-Akashi	1995	6.9	0.371	0.174	0.148	0.040
3	Kobe, Japan	JR Takatori	1995	6.9	0.272	0.162	0.252	0.225
4	Northridge, USA	Beverly Hills—14145 Mulholland Drive	1994	6.7	0.319	0.201	0.311	0.057
5	Northridge, USA	Canyon Country—W Lost Cany	1994	6.7	0.286	0.189	0.194	0.299
6	Kobe, Japan	Shin–Osaka	1995	6.9	0.059	0.065	0.089	0.048
7	Izmit-Kocaeli, Turkey	Arcelik	1999	7.4	0.079	0.082	0.082	0.040
8	Landers, USA	Yermo Fire Station	1992	7.3	0.136	0.132	0.222	0.059
9	Loma Prieta, USA	Capitola	1989	6.9	0.510	0.194	0.227	0.043
10	Loma Prieta, USA	Gilroy Array #3	1989	6.9	0.369	0.448	0.410	0.369
11	Manjil, Iran	Abbar	1990	7.4	0.538	0.448	0.563	0.248
12	Cape Mendocino, USA	Rio Dell Overpass–FF	1992	7.0	0.195	0.104	0.263	0.100
13	Chi-Chi, Taiwan	CHY101	1999	7.6	0.156	0.274	0.199	0.180
14	Chi-Chi, Taiwan	TCU045	1999	7.6	0.339	0.201	0.270	0.131
15	Lytle Creek, USA	Wrightwood Park	1970	5.3	0.054	0.045	0.030	0.004
16	Livermore-02, USA	Liv.-Morgan TP	1980	5.4	0.079	0.035	0.079	0.005
17	Chi-Chi, Taiwan	CHY006	1999	7.6	0.216	0.232	0.327	0.244
18	NW China-03	Jiashi	1997	6.1	0.384	0.102	0.104	0.030
19	Kobe, Japan	Kakogawa	1995	6.9	0.158	0.107	0.257	0.055
20	Hollister-03, USA	Hollister City Hall	1974	5.1	0.068	0.030	0.020	0.011
21	Kozani, Gr-02, Greece	Chromio	1995	5.1	0.072	0.023	0.007	0.000
22	Loma Prieta, USA	SF Intern. Airport	1989	6.9	0.065	0.056	0.121	0.033
23	Loma Prieta, USA	Fremont, Mission	1989	6.9	0.083	0.092	0.178	0.024
24	Northridge, USA	Arleta—Nordhoff	1994	6.7	0.552	0.178	0.260	0.194
25	Whittier, USA	Whittier Dam	1987	5.7	0.532	0.101	0.071	0.024
26	San Fernando, USA	Pacoima Dam	1971	6.6	0.710	0.585	0.350	0.332
27	Chi-Chi, Taiwan	TCU065	1999	7.6	0.263	0.706	0.444	0.411
28	Kobe, Japan	Takarazuka	1995	6.9	0.433	0.354	0.405	0.196
29	Kobe, Japan	Takatori	1995	6.9	0.272	0.162	0.252	0.225
30	Loma Prieta, USA	Saratoga	1989	6.9	0.361	0.272	0.297	0.158
31	Northridge, USA	Rinaldi	1994	6.7	0.847	0.159	0.088	0.040
32	Northridge, USA	Newhall	1994	6.7	0.548	0.313	0.332	0.098
33	Northridge, USA	Converter	1994	6.7	0.535	0.389	0.310	0.181
34	Northridge, USA	W. Pico Canyon	1994	6.7	0.286	0.294	0.414	0.151
35	Superstition Hills, USA	Wildlife Liquef	1987	6.6	0.423	0.055	0.103	0.037
36	Tabas, Iran	Tabas	1978	7.4	0.746	0.415	0.653	0.254
37	Kobe, Japan	KJMA	1995	6.9	0.343	0.391	0.658	0.294
38	Imperial Valley-06	Bonds Corner	1979	6.5	0.355	0.127	0.218	0.068
39	Imperial Valley-06	El Centro Array #5	1979	6.5	0.479	0.469	0.182	0.195
40	Imperial Valley-06	El Centro Array #6	1979	6.5	1.644	0.581	0.439	0.246
41	Imperial Valley-06	El Centro Array #7	1979	6.5	0.472	0.279	0.323	0.230

Table 3. *Cont.*

Number	Earthquake	Station	Year	Magnitude	PGA (g)	PGV (m/s)	$S_{a\text{-}1s}$ (g)	$S_{a\text{-}2s}$ (g)
42	Imperial Valley-06	El Centro Array #8	1979	6.5	0.356	0.250	0.193	0.149
43	Imperial Valley-06	El Centro Differential Array	1979	6.5	0.464	0.275	0.183	0.123
44	Imperial Valley-06	Holtville Post Office	1979	6.5	0.209	0.149	0.067	0.074
45	Kobe, Japan	Port Island (0 m)	1995	6.9	0.562	0.718	0.505	0.670
46	Izmit-Kocaeli, Turkey	Yarimca	1999	7.4	0.241	0.325	0.327	0.497
47	Northridge, USA	Jensen Filter Plant Administrative Building	1994	6.7	0.401	0.412	0.509	0.280
48	Northridge, USA	Sylmar—Converter Sta East	1994	6.7	0.494	0.265	0.290	0.276
49	Nahanni, Canada	Site 1	1985	6.8	2.370	0.421	0.457	0.231
50	Nahanni, Canada	Site 3	1985	6.8	0.182	0.158	0.085	0.084
51	Cape Mendocino, USA	Cape Mendocino	1992	7.0	0.754	0.781	0.394	0.227
52	Northridge, USA	Jensen Filter Plant Generator Building	1994	6.7	0.760	0.329	0.511	0.201
53	Northridge, USA	Los Angeles Dam	1994	6.7	0.323	0.260	0.271	0.124
54	Northridge, USA	Pacoima Kagel Canyon	1994	6.7	0.180	0.144	0.260	0.206
55	Northridge, USA	Arleta—Nordhoff Fire Sta	1994	6.7	0.552	0.178	0.260	0.194
56	Northridge, USA	Newhall—W Pico Canyon Rd.	1994	6.7	0.286	0.294	0.414	0.151
57	Northridge, USA	Rinaldi Receiving Sta	1994	6.7	0.847	0.477	0.516	0.208
58	Northridge, USA	Sylmar—Converter Sta Valve Group 1–6	1994	6.7	0.535	0.389	0.310	0.181
59	Northridge, USA	Sylmar—Converter Sta Valve Group 7	1994	6.7	0.787	0.429	0.533	0.233

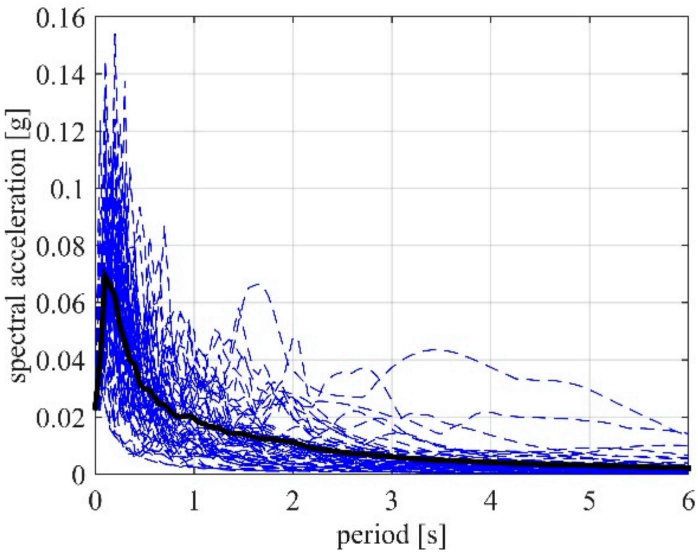

Figure 11. The response spectra (dashed lines) and average spectrum (bold solid line) of 59 scaled vertical ground motions (scaled PGA is 0.023 g).

4. Influence of Vertical Ground Motion on Crowd-Induced Vibration of Footbridge

In this section, the footbridge subjected to earthquake loads is firstly given. Next, the vibration levels are calculated for the case with both crowd loads and earthquake loads. Because of the limited space available in this paper, the numerical results of the earthquakes with intensity 7 are provided as an illustration.

4.1. Footbridge Vibration Induced by Earthquake Loads

In this subsection, the footbridge is only subjected to earthquake loads. The earthquake loads described in Section 3 are applied to calculate the induced vibrations of the illustrative structure. In the response calculation, considering the 'rich' frequency contents of the seismic inputs, the contributions from the first five vertical modes are considered. The earthquakes can occur at a random time instant t_{eq} within the relevant total simulation time span.

Figure 12 illustrates the time history of the structural acceleration responses in the vertical direction subjected to the Kobe Earthquake (intensity 7), which is assumed to occur at time instant $t_{eq} = 0$ s for the illustrative example. The maximum acceleration amplitude reached 1.81 m/s^2.

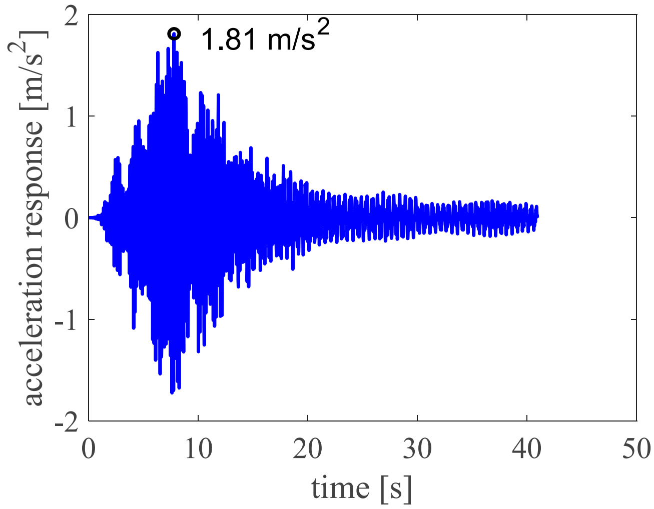

Figure 12. The time history of the structural acceleration responses in the vertical (Z) direction subjected to the Kobe Earthquake (intensity 7), which occurs at time instant $t_{eq} = 0$ s.

Figure 13 shows the empirical cumulative distribution function (CDF) based on the 59 maximum acceleration amplitudes induced by different ground accelerations which are assumed to occur at time instant $t_{eq} = 0$ s. As shown in Figure 13, most amplitudes ranged from 0.39 to 3.07 m/s^2.

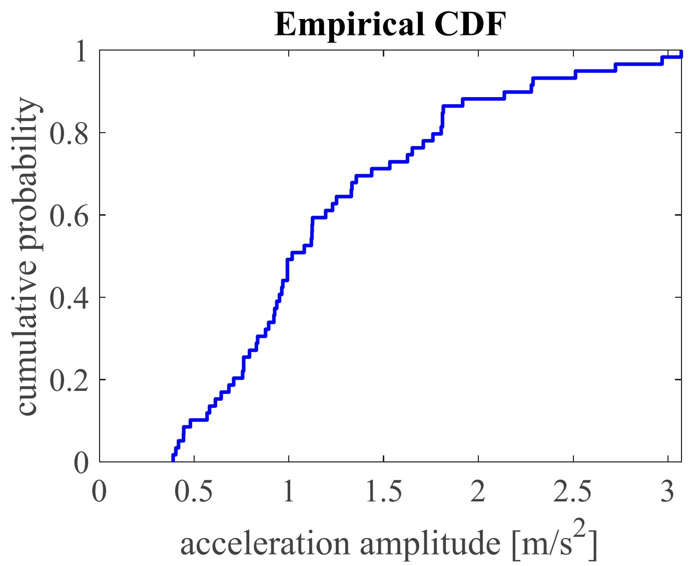

Figure 13. An empirical cumulative distribution function (CDF) plotted by the 'cdfplot' Matlab function, based on the 59 maximum acceleration amplitudes (intensity 7 as an example) induced by different ground accelerations in the vertical (Z) direction.

4.2. Footbridge Vibration Induced by Crowd Loads and Earthquake Loads

This subsection investigates the case that the footbridge is subjected to both crowd loads and earthquake loads. The induced total response is a combination of the vibrations due to crowd loads and earthquake loads. Theoretically, an earthquake can occur at any time during the crowd passing. To consider the randomness of the earthquake occurring at time instant t_{eq}, it can be considered as:

$$0\ \mathrm{s} \le t_{\mathrm{eq}} \le t_{\mathrm{last}} \tag{8}$$

where t_{last} is the arrival time of the last person in the crowd, e.g., for the illustrative example, $t_{\mathrm{last}} = t_{25} = 34.86$ s for 0.1 pedestrians/m^2 and $t_{\mathrm{last}} = t_{375} = 61.74$ s for 1.5 pedestrians/m^2. The time is long enough for the structural responses to reach maxima. Furthermore, a time shift of 0.02 s is adopted for each pair of two different neighbouring t_{eq}.

Figure 14 depicts the maximum amplitudes in the time history of the total structural acceleration responses in the vertical direction subjected to crowd loads and the Kobe Earthquake (intensity 7) that occur at a different time instant t_{eq}. The combined structural responses are significantly affected by the time instant t_{eq} for all density cases. The maximum amplitudes of the total responses are 2.01, 2.11, 2.25, 2.14, 2.27, and 2.52 m/s^2 for the responses induced by the earthquake and the six crowds with different densities. For the same earthquake, the maximum amplitude does not increase linearly with the density.

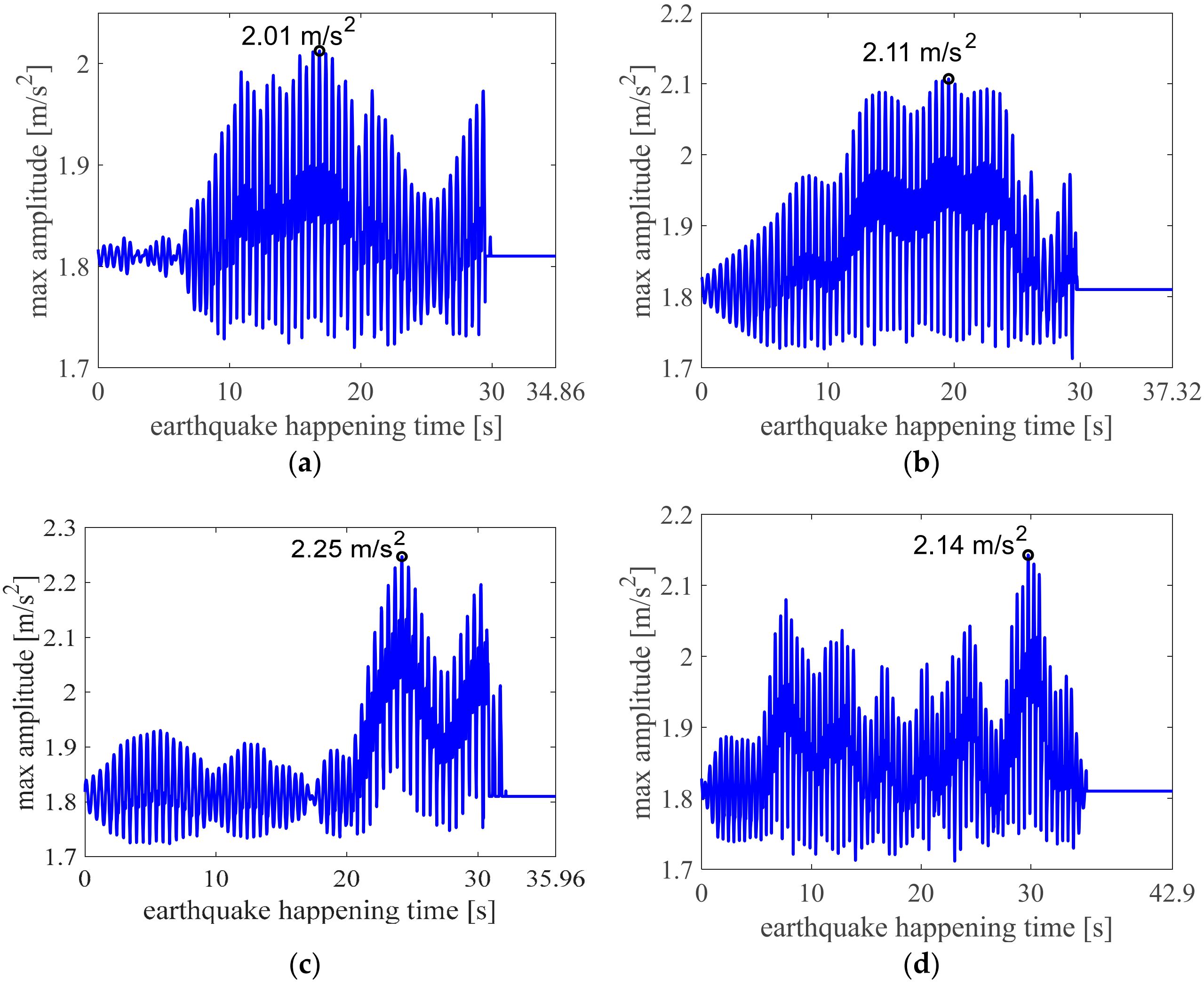

Figure 14. *Cont.*

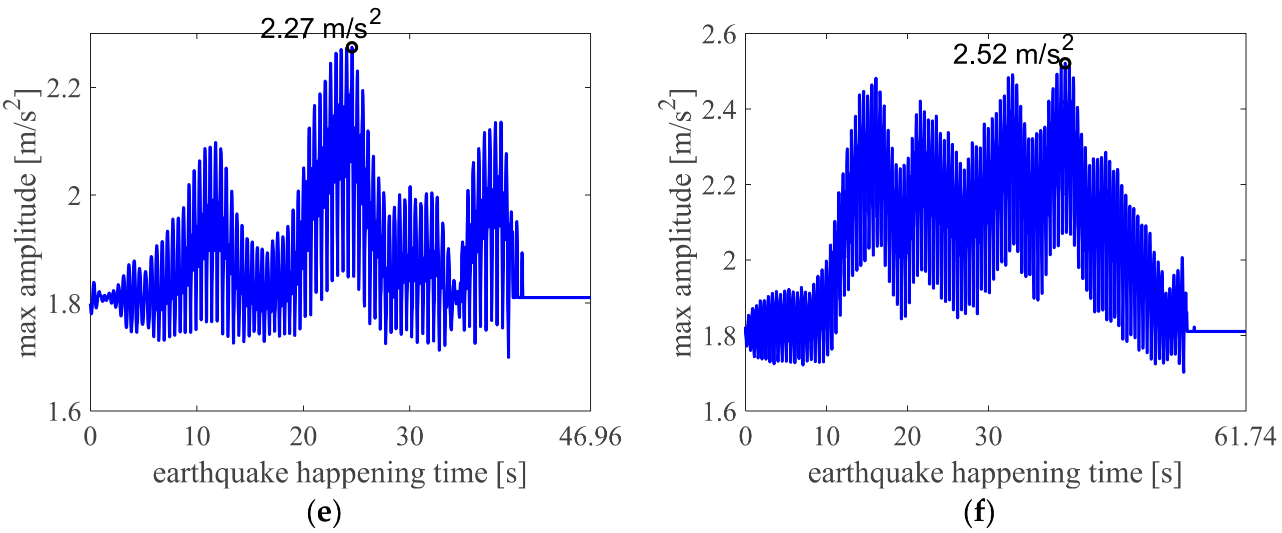

Figure 14. The maximum amplitudes in the time history of the total structural acceleration responses in the vertical (Z) direction to the crowd and the Kobe Earthquake (intensity 7 as an example) that occurs at different time instants t_{eq}. (**a**) 0.1 pedestrians/m^2, (**b**) 0.2 pedestrians/m^2, (**c**) 0.5 pedestrians/m^2, (**d**) 0.8 pedestrians/m^2, (**e**) 1.0 pedestrians/m^2, (**f**) 1.5 pedestrians/m^2.

Figure 15 presents the empirical cumulative distribution functions (CDFs) based on 7 times of 59 maximum acceleration amplitudes induced by different ground accelerations (1 time) and by both earthquake and crowd loads (6 times). The cases with both the crowd and earthquake loads basically have much higher acceleration amplitudes than the cases with crowd load or earthquake load only. As expected, the lowest and the highest acceleration amplitude curves are obtained by the cases with a low density of 0.1 pedestrians/m^2 and high density of 1.5 pedestrians/m^2, respectively. However, the amplitudes do not increase with density and there exists a valley for the case with 0.8 pedestrians/m^2. For the densities in between, the case with a lower density of 0.2 pedestrians/m^2 may induce even higher acceleration amplitudes than the case with 0.8 pedestrians/m^2.

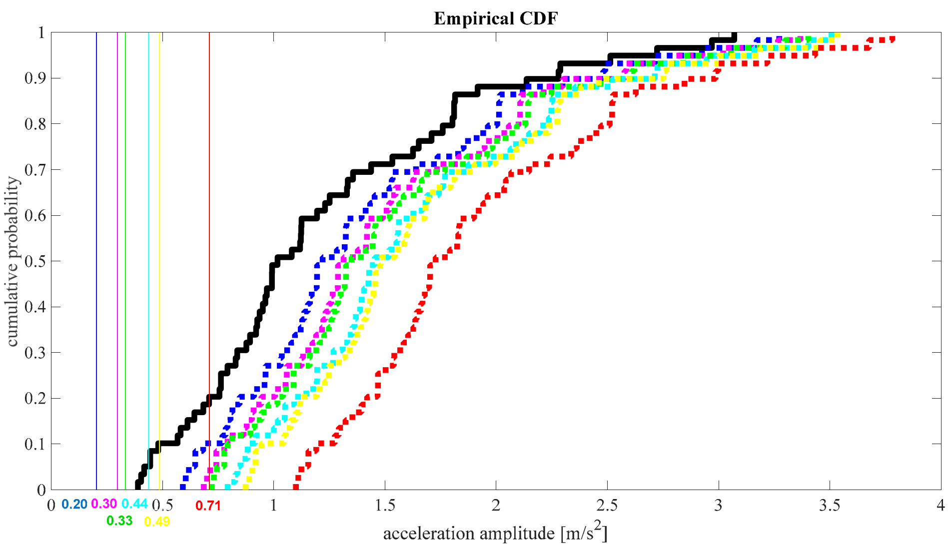

Figure 15. Empirical cumulative distribution functions (CDFs) based on 7 times of 59 maximum acceleration amplitudes (intensity 7) induced by different ground accelerations (1 black wide solid curve) and by both earthquake and crowd loads (6 dashed curves: the blue wide dashed curve for low density of 0.1 pedestrians/m^2, the red dotted wide curve for high density of 1.5 pedestrians/m^2, and other dashed curves for other densities: pink for 0.2, green for 0.8, cyan for 0.5, yellow for 1.0).

For comparison, six additional vertical straight lines are added as the induced maximum responses by the low density of 0.1 pedestrians/m^2 crowd (the blue narrow solid line of 0.20 m/s^2), the high density of 1.5 pedestrians/m^2 (red narrow solid line of 0.71 m/s^2) crowd, and four other density cases (pink for 0.2, green for 0.8, cyan for 0.5, yellow for 1.0).

5. Amplification Effects of Vertical Ground Motion

5.1. Amplification Factors of Structural Responses Due to Ground Motion

To quantify the effects of the ground motion on the structural response subjected to crowd loads and earthquake loads, an amplification factor is introduced as the ratio of maximum acceleration responses to combined loads (both crowd and earthquake) and crowd loads only. In total, there are 195,408 (= 138 $\times$ 6 $\times$ 59 $\times$ 4) calculation cases for 138 footbridges, 6 pedestrians' densities, and 59 vertical ground motions with 4 intensities. In some calculation cases, the input parameters are incomplete and have been removed. As a result, 171,572 datasets are finally selected. Table 4 shows the statistical values of amplification factors for different earthquake intensities. As shown in Table 4, the effects of higher earthquake intensity are generally larger than those of the corresponding lower earthquake intensity. It is characterized by higher mean values of the amplification factor because larger vibration responses are caused by earthquakes with higher intensity. The scatter (characterized with standard deviation) is also larger for higher earthquake intensity. This results from the fact that when the pedestrian-induced vibration levels are kept constant, the contribution of the ground motion in the structural responses is reasonably more significant for earthquakes with higher intensity. Consequently, the amplification factor is more easily affected by the randomness of the ground motion. In other words, relatively higher vibration levels induced by the earthquake can result in high mean and standard deviation values for the amplification factor. This can also be supported by the observations in Table 5. Generally, higher mean and standard deviation amplification factor values are found for lower acceleration amplitudes induced by the crowd, when the earthquake intensity is kept constant (intensity 7). It is also notable that the basic trend is slightly altered due to random characteristics of crowd loads. This is because the amplification factor is not only determined by earthquake loads but also by crowd loads.

Table 4. Statistical values of amplification factor for different earthquake intensities.

Earthquake Intensity	Maximum	Minimum	Mean	St.D.
6	165.98	1.00	5.30	6.84
7	322.29	1.00	9.42	13.29
8	645.96	1.00	17.96	26.64
9	1290.53	1.00	34.97	53.24

Table 5. Statistical values of amplification factor for different densities in the case of intensity 7.

Density (Pedestrians/m^2)	Acceleration Amplitude Induced by Crowd Loads (m/s^2)	Mean	St.D.
0.1	0.20	2.26	0.63
0.2	0.30	1.87	0.44
0.5	0.44	1.69	0.35
0.8	0.33	2.26	0.64
1.0	0.49	1.70	0.36
1.5	0.71	1.66	0.33

The amplification factor is governed by the structure, the crowd, and the earthquake, so the structural-related, crowd-related, and earthquake-related parameters are defined as inputs and the amplification factor is taken as an output. Ten parameters, including four structure-related parameters, one crowd-related parameter, and five earthquake-related parameters, are taken as the input variables, with the amplification factor taken as the only output variable. The statistical values of the input and output variables are listed in Table 6.

Table 6. Statistical values of input and output variables.

Variable Type	Parameters		Unit	Maximum	Minimum	Mean	St.D.
Input	Structure-related	L	m	230.00	4.80	38.94	28.45
		W	m	13.35	0.78	2.76	1.51
		$M_{1,v}$	kg	724,500.00	922.74	64,781.25	76,013.95
		ξ	%	2.50	0.40	0.95	0.66
Input	Crowd-related	ρ_{crowd}	pedestrians/m^2	1.50	0.10	0.67	0.47
Input	Earthquake-related	Scaled PGA	g	0.09	0.01	0.04	0.03
		Original PGA	g	2.37	0.05	0.44	0.38
		Original PGV	m/s	0.78	0.02	0.27	0.18
		Original $S_{a\text{-}1s}$	g	0.66	0.01	0.28	0.16
		Original $S_{a\text{-}2s}$	g	0.67	0.00	0.17	0.13
Output		Amplification factor	-	1290.53	1.00	16.91	32.73

Figure 16 plots the relationship between the amplification factor and 10 input variables. It shows that the scaled PGA, which is closely related to seismic intensity, has an obvious positive correlation with the amplification factor. With the increase of the main span L, there is a general trend that the amplification factor increases. Conversely, the amplification factor has a descending tendency with the increase of the damping ratio ξ and pedestrian density ρ_{crowd}. There are no significant correlations between the remaining parameters and the amplification factor.

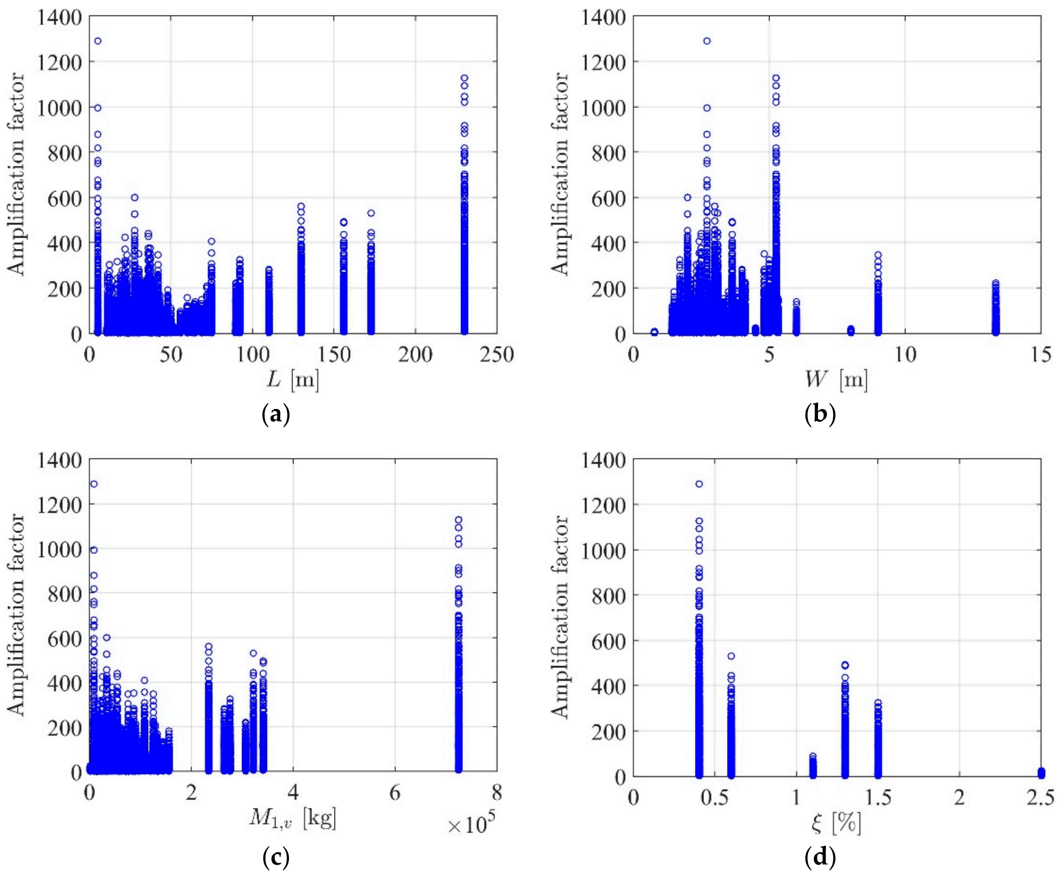

Figure 16. *Cont.*

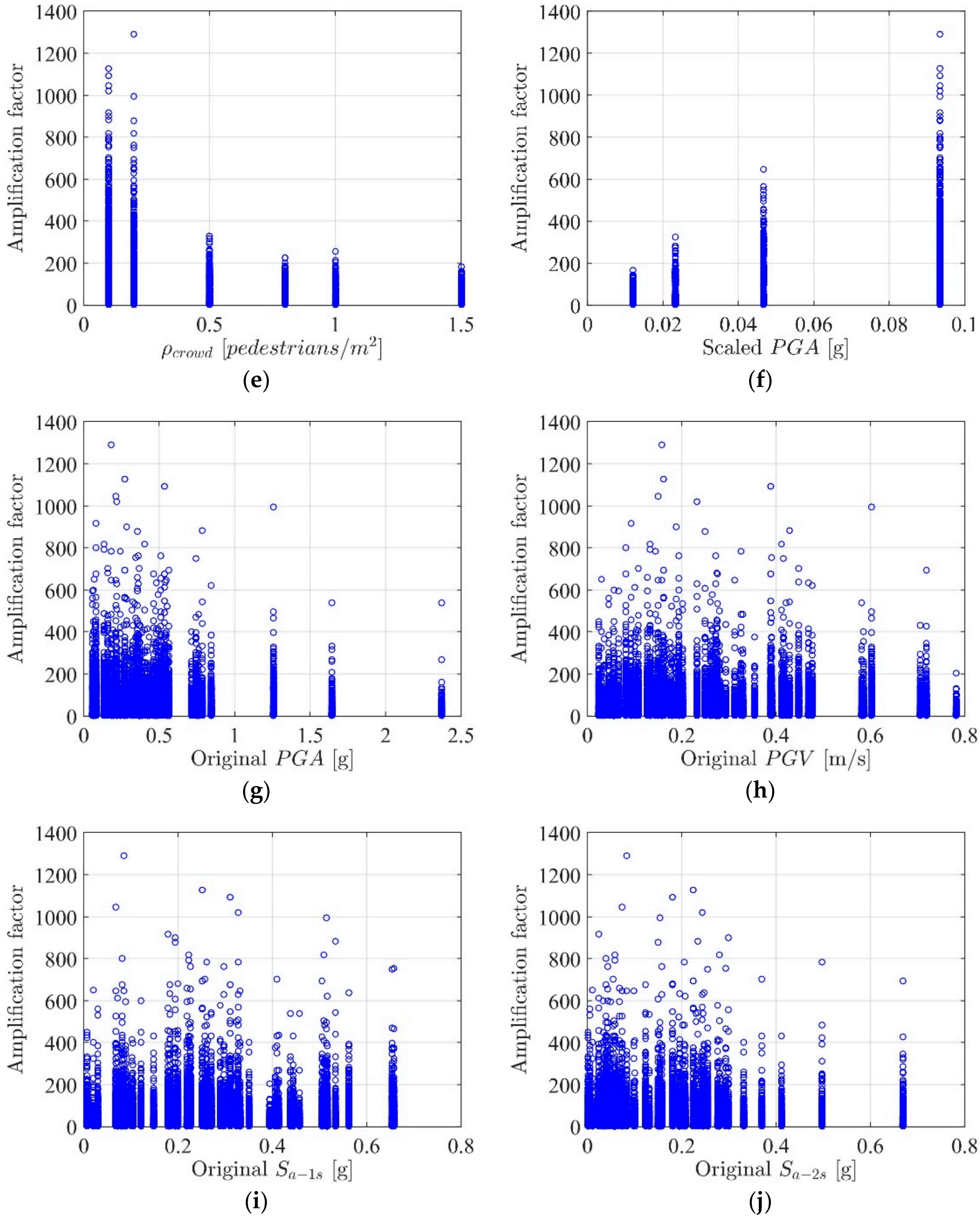

Figure 16. Relationship between the amplification factor and 10 input variables. (**a**) Input 1, (**b**) Input 2, (**c**) Input 3, (**d**) Input 4, (**e**) Input 5, (**f**) Input 6, (**g**) Input 7, (**h**) Input 8, (**i**) Input 9, (**j**) Input 10.

5.2. Machine Learning (ML)-Based Prediction of Amplification Factor

As there exists a strong nonlinear relationship between the inputs and output, machine-learning (ML) techniques, which are suitable for solving the nonlinear regression problem, are used to predict the amplification factor. Two individual-type ML algorithms, i.e., decision tree (DT) and artificial neural network (ANN), and two ensemble ML algorithms, i.e., random forest (RF) and gradient boosting regression tree (GBRT), are adopted to construct the predictive models. The characteristics of the four ML algorithms are briefly summarized as follows.

The most widely used DT algorithm is the classification and regression tree (CART). By using the CART, a characteristic space can be separated into several units. Each unit corresponds to an output. Based on the characteristic of any testing data, it can be designated into a unit and then acquire the output. The DT often has an over-fitting issue and the drawback of processing missing data. The ANN algorithm consists of a large number of neurons or processing elements arranged in different layers. The idea of the ANN originates from the biological nervous systems. A neural network becomes a vector mapper which maps input vectors to an output vector. The RF is a famous bagging-type ensemble learning algorithm based on the DT. The principle of the bagging approach is to separate the training dataset into m new training datasets and generate an independent model for each training dataset. As for the RF, m training datasets can be created by the bootstrap approach. A DT is then generated for each training dataset. The over-fitting issue can be avoided by using the RF. The GBRT is a widely used boosting-type ensemble learning algorithm. It uses a negative gradient of loss function to represent the residual error. By integrating different weaker learners, the GBRT can decrease the deviation and maintain the low variance of the weaker learners.

As mentioned in Section 5.1, a database including 171,572 datasets is used to train and test the ML algorithms. As a common practice [77], 70% and 30% of the data are used as the training and testing datasets, respectively. The Bayesian optimization method is adopted to determine the optimized hyper-parameters of the ML algorithms. The optimized parameters of the four ML algorithms are listed in Table 7.

The predictive accuracy of the ML algorithms is quantitatively evaluated by three widely used performance indices, i.e., coefficient of determination R-squared (R^2), root mean square error (RMSE), and mean absolute error (MAE):

$$\mathrm{R}^2 = 1 - \frac{\sum_{i=1}^{N}(C_i - P_i)^2}{\sum_{i=1}^{N}(C_i - \overline{C})^2} \tag{9}$$

$$\mathrm{RMSE} = \sqrt{\frac{\sum_{i=1}^{N}(C_i - P_i)^2}{N}} \tag{10}$$

$$\mathrm{MAE} = \frac{\sum_{i=1}^{N}|C_i - P_i|}{N} \tag{11}$$

where C_i and P_i are the calculated and predicted values, respectively; N is the number of datasets in the database; and $\overline{C}$ is the average calculated value. A good predictive model requires that its R^2 is close to 1 and its RMSE and MAE are small.

The performance measures of the four ML algorithms are tabulated in Table 8. Figure 17 illustrates the relationship of the predicted values and the reference values for both the training and testing datasets.

It can be concluded from Table 8 and Figure 17 that the two ensemble algorithms have a better predictive performance than the two individual ML algorithms. In terms of the performance measures of the testing dataset, the best predictive model is GBRT, whose R^2 is closest to 1 and RMSE and MAE are the smallest. Based on the GBRT model, the feature importance [49,50] is conducted to quantify the importance of different features (input variables) on the amplification factor. The relative feature importance of all input variables is plotted in Figure 18. It can be concluded from Figure 18 that the scaled PGA (earthquake-related), ρ_{crowd} (crowd-related), and L (structure-related) are the three most important features, while the influence of W on the amplification factor is less significant.

Table 7. Optimized parameters of the four ML algorithms.

ML Algorithm	Parameters
ANN	activation = 'tanh' alpha = 0.3030395941208759 hidden_layer_sizes = 493 max_iter = 496 random_state = 5 solver = 'lbfgs'
DT	criterion = 'friedman_mse' max_depth = 29 max_features = 9 min_samples_leaf = 6 min_samples_split = 12 random_state = 5
GBRT	Criterion = 'mse' learning_rate = 0.3830013954408691 loss = 'lad' max_depth = 9 max_features = 7 min_samples_leaf = 11 min_samples_split = 11 n_estimators = 285
RF	max_depth = 25 max_features = 7 min_samples_leaf = 2 min_samples_split = 5 n_estimators = 169 random_state = 5

Table 8. Performance measures of four ML algorithms.

ML Algorithm	Datasets	Performance Indices		
		R^2	RMSE	MAE
DT	Training	0.890	10.75	3.72
	Testing	0.780	15.62	5.18
ANN	Training	0.837	13.11	6.04
	Testing	0.791	15.23	6.25
RF	Training	0.942	7.83	2.54
	Testing	0.823	14.04	4.21
GBRT	Training	0.923	9.02	2.33
	Testing	0.870	12.00	3.00

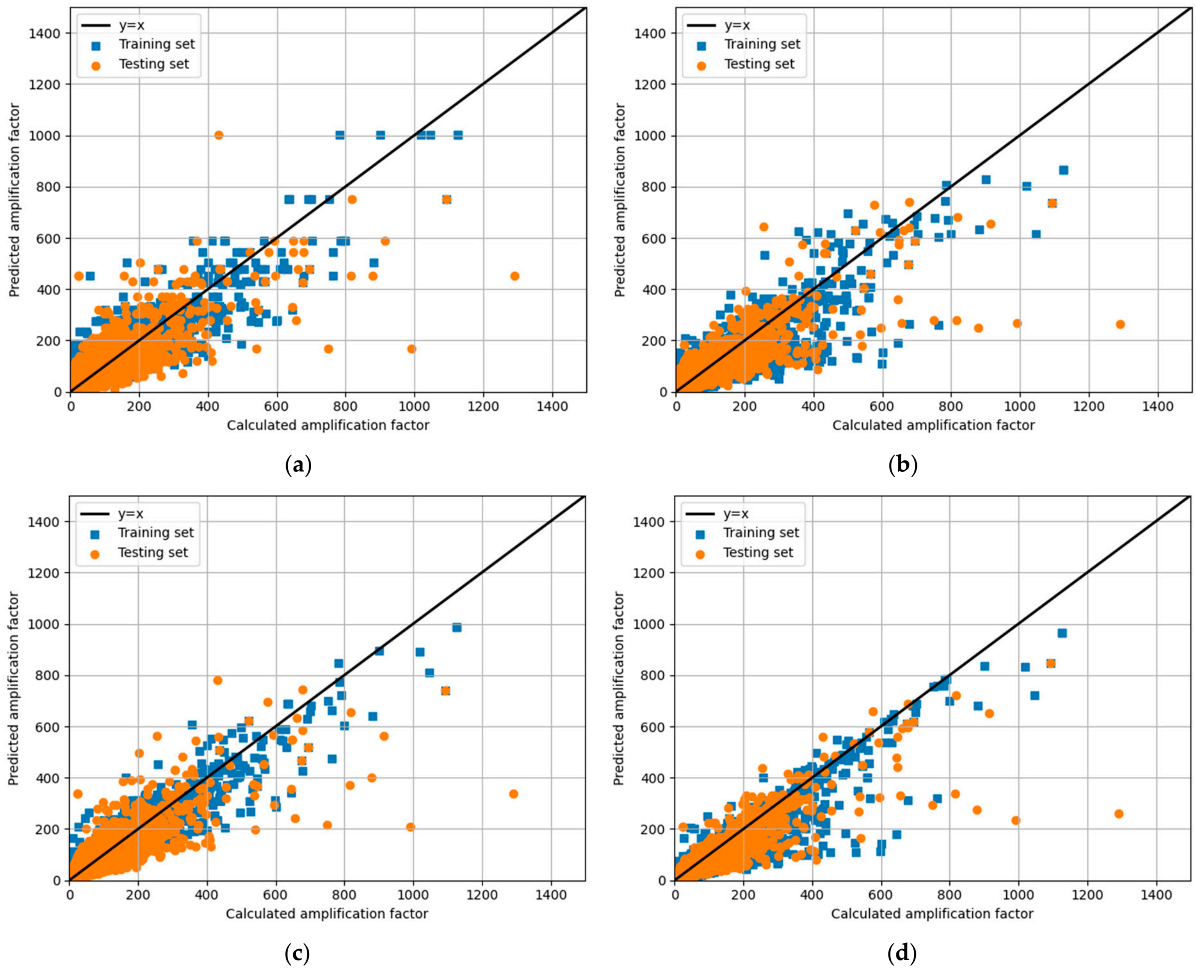

Figure 17. Prediction results of amplification factor using four ML algorithms. (**a**) DT, (**b**) ANN, (**c**) RF, (**d**) GBRT.

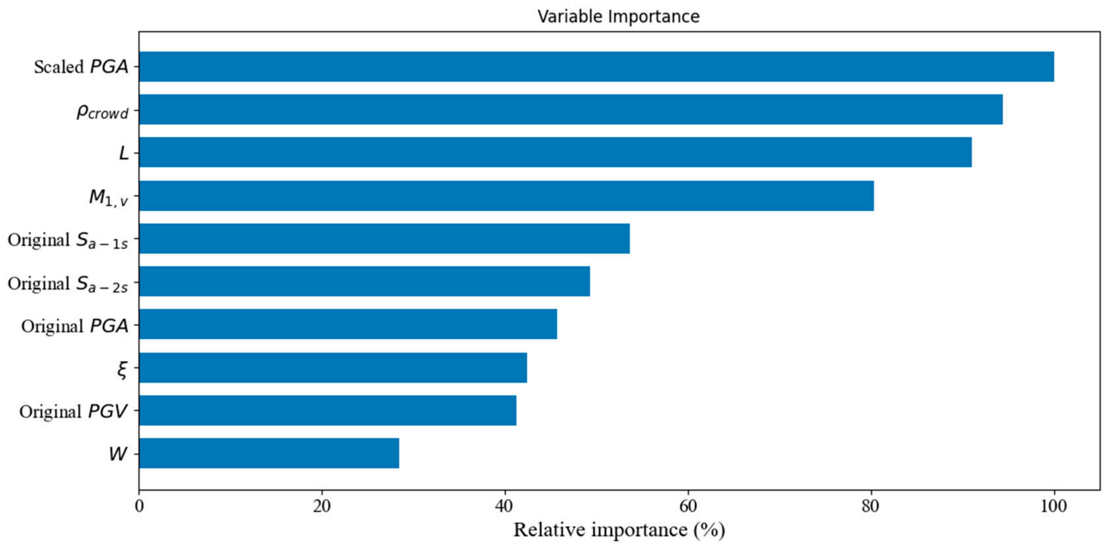

Figure 18. Relative importance of all features (input variables).

6. Vibration Serviceability Evaluation

For the case with earthquake intensity 7, the results are presented in Figure 15. It can be concluded from the empirical cumulative distribution function plot (Figure 15) that when the structure is only subjected to vertical ground motions, there is approximately

50% probability that the vibration levels fall into the range of the minimum comfort limits of 1.0–2.5 m/s^2 according to Setra and HiVoSS, with the probability of the vibration levels exceeding the human comfort limits in the vertical direction (2.5 m/s^2) being very low according to HiVoSS. For crowd load only, the acceleration level is always lower than the comfort limits. When the structure is subjected to earthquake and pedestrian walking by a low-density crowd, the exceedance probability to the human comfort limits is approximately 10%. For high-density crowd evacuation during an earthquake, the corresponding exceedance probability is approximately 20%. However, when recalling the amplification factor values for different earthquake intensities (Table 4), the mean values of the amplification factor are 1.91 (=17.96/9.42) and 3.71 (=34.97/9.42) times higher for intensities of 8 and 9, respectively. Correspondingly, the acceleration amplitudes can be nearly doubled and quadrupled, leading to the acceleration levels exceeding the comfort limits at all or most times, which is very risky for human evacuation and may even result in pedestrians falling. Thus, the serviceability of the footbridge may be impeded.

7. Conclusions

There is no existing research considering the combined effects caused by human-induced loads and vertical ground motions of footbridges. To fill the gap, this paper investigates the effects of vertical ground motion on human-induced vibrations of footbridges. A total of 138 footbridges with different materials, dimensions, and structural types are taken as the target structures. The social force model combined with the pedestrian-induced force model is applied to simulate crowd loads with six representative pedestrian densities as required by design codes. Fifty-nine vertical ground motions with four seismic intensities are adopted as the seismic inputs. The amplification factor is defined to quantify the amplification effects of vertical ground motion on human-induced vibrations of footbridges. Four ML algorithms are used to predict the amplification factor. The vibration serviceability of the footbridge subjected to both crowd load and vertical ground motion is also assessed. Several conclusions can be drawn as follows:

1. The scaled PGA has an obvious positive correlation with the amplification factor. With the increasing of the main span L, there is a general trend of the amplification factor increasing. Conversely, the amplification factor has a descending tendency with the increase of the damping ratio ξ and pedestrian density ρ_{crowd}. There is no significant correlation between the remaining parameters and the amplification factor.
2. The amplification factor is governed by structure-related, crowd-related, and earthquake-related parameters. The scaled PGA, the pedestrian density, and the bridge span are the most important parameters determining the amplification factor.
3. For the considered load scenarios in this paper, when the footbridges are only subjected to crowd loads or the vertical ground motions, there is a very small probability that the vibration levels exceed the upper limit (2.5 m/s^2) of the minimum human comfort limits in a vertical direction as suggested by current design codes. However, it is worthwhile to note that the vibration levels can be different for other cases. Furthermore, comfort limits can be also changed by, e.g., the degree of mutual synchronization of pedestrians in the crowd and their synchronization with the natural frequency of the structure, depending on the value of this frequency.
4. With both the crowd and earthquake loads considered, the acceleration levels may exceed the comfort limits. In particular, when the earthquake intensity is larger than 7, the vibration amplitudes to the combined loads may be higher than the comfort limits at all or most times, which is very risky for human evacuation and may even result in pedestrians falling. Thus, the serviceability of the footbridge may be impeded.

This study may urge footbridge designers to consider the scenario where the crowds are evacuated in earthquakes. A first estimation of the induced vibration levels to the combined loads can be obtained by considering the amplification factor for different crowd densities and earthquakes with different intensities.

In future work, more realistic evacuation scenarios can be simulated by considering possible running persons for the low crowd density cases and pedestrian–structure interactions during earthquakes. Furthermore, the simulations can be more realistic if real-world data for pedestrian evacuation in earthquakes are available.

Author Contributions: Conceptualization, X.W. and B.F.; methodology, X.W. and B.F.; validation, X.W. and B.F.; investigation, X.W. and B.F.; data curation, X.W., B.F., W.W. and X.L.; writing—original draft preparation, X.W.; writing—review and editing, B.F. and W.W.; funding acquisition, B.F. All authors have read and agreed to the published version of the manuscript.

Funding: This research was funded by the National Natural Science Foundation of China (Grant No. 51908048), the Young Talent Fund of University Association for Science and Technology in Shaanxi, China (Grant No. 20200412), and the Natural Science Foundation of Shaanxi Province (Grant No. 2021JM-179).

Informed Consent Statement: Not applicable.

Data Availability Statement: Some or all data, models, or code that support the findings of this study are available from the corresponding author upon reasonable request.

Conflicts of Interest: The authors declare no conflict of interest.

References

1. Dallard, P.; Fitzpatrick, A.J.; Flint, A.; Le Bourva, S.; Low, A.; Ridsdill, R.M.; Willford, M. The London Millennium Footbridge. *Struct. Eng.* **2001**, *79*, 17–33.
2. Ingólfsson, E.T.; Georgakis, C.T. A stochastic load model for pedestrian-induced lateral forces on footbridges. *Eng. Struct.* **2011**, *33*, 3454–3470. [CrossRef]
3. Racic, V.; Brownjohn, J.M.W. Mathematical modelling of random narrow band lateral excitation of footbridges due to pedestrians walking. *Comput. Struct.* **2012**, *90–91*, 116–130. [CrossRef]
4. Bruno, L.; Corbetta, A. Uncertainties in crowd dynamic loading of footbridges: A novel multi-scale model of pedestrian traffic. *Eng. Struct.* **2017**, *147*, 545–566. [CrossRef]
5. Casciati, F.; Casciati, S.; Faravelli, L. A contribution to the modelling of human induced excitation on pedestrian bridges. *Struct. Saf.* **2017**, *66*, 51–61. [CrossRef]
6. Bruno, L.; Venuti, F. A simplified serviceability assessment of footbridge dynamic behaviour under lateral crowd loading. *Struct. Eng. Int.* **2010**, *20*, 442–446. [CrossRef]
7. Živanović, S. Benchmark footbridge for vibration serviceability assessment under the vertical component of pedestrian load. *J. Struct. Eng.* **2012**, *138*, 1193–1202. [CrossRef]
8. Setareh, M. Vibration serviceability issues of slender footbridges. *J. Bridge Eng.* **2016**, *21*, 04016084. [CrossRef]
9. Bedon, C. Diagnostic analysis and dynamic identification of a glass suspension footbridge via on-site vibration experiments and FE numerical modelling. *Compos. Struct.* **2019**, *216*, 366–378. [CrossRef]
10. Feng, P.; Wang, Z.; Jin, F.; Zhu, S. Vibration serviceability assessment of pedestrian bridges based on comfort level. *J. Perform. Constr. Facil.* **2019**, *33*, 04019046. [CrossRef]
11. Fu, B.; Wei, X. An intelligent analysis method for human-induced vibration of concrete footbridges. *Int. J. Struct. Stab. Dyn.* **2021**, *21*, 2150013. [CrossRef]
12. Gong, M.; Shen, R.; Li, Y.; Wang, H.; Chen, W.; Wei, X. Practical suggestions for specifications in vibration serviceability of footbridges based on two recent long-span footbridges. *Struct. Eng. Int.* **2022**, *in press*. [CrossRef]
13. Morbiato, T.; Vitaliani, R.; Saetta, A. Numerical analysis of a synchronization phenomenon: Pedestrian–structure interaction. *Comput. Struct.* **2011**, *89*, 1649–1663. [CrossRef]
14. Carroll, S.; Owen, J.; Hussein, M. Modelling crowd–bridge dynamic interaction with a discretely defined crowd. *J. Sound Vib.* **2012**, *331*, 2685–2709. [CrossRef]
15. Jiménez-Alonso, J.F.; Sáez, A.; Caetano, E.; Magalhães, F. Vertical Crowd–Structure Interaction Model to Analyze the Change of the Modal Properties of a Footbridge. *J. Bridge Eng.* **2016**, *21*, C4015004. [CrossRef]
16. Shahabpoor, E.; Pavic, A.; Racic, V. Structural vibration serviceability: New design framework featuring human-structure interaction. *Eng. Struct.* **2017**, *147*, 295–311. [CrossRef]
17. Toso, M.A.; Gomes, H.M.; Vital de Brito, J.L. Crowd-structure interaction: Investigating the spatiality and synchronization of a pedestrian force model. *J. Bridge Eng.* **2017**, *133*, 510–521. [CrossRef]
18. Mulas, M.G.; Lai, E.; Lastrico, G. Coupled analysis of footbridge-pedestrian dynamic interaction. *Eng. Struct.* **2018**, *176*, 127–142. [CrossRef]
19. Setareh, M.; Gan, S. Vibration testing, analysis, and human-structure interaction studies of a slender footbridge. *J. Perform. Constr. Facil.* **2018**, *32*, 04018068. [CrossRef]

20. Ahmadi, E.; Caprani, C.; Živanović, S.; Heidarpour, A. Assessment of human-structure interaction on a lively lightweight GFRP footbridge. *Eng. Struct.* **2019**, *199*, 109687. [CrossRef]
21. Caetano, E.; Cunha, Á.; Moutinho, C.; Magalhães, F. Studies for controlling human-induced vibration of the Pedro e Inês footbridge, Portugal. Part 2: Implementation of tuned mass dampers. *Eng. Struct.* **2010**, *32*, 1082–1091. [CrossRef]
22. Li, Q.; Fan, J.; Nie, J.; Li, Q.; Chen, Y. Crowd-induced random vibration of footbridge and vibration control using multiple tuned mass dampers. *J. Sound Vib.* **2010**, *329*, 4068–4092. [CrossRef]
23. Casado, C.M.; Díaz, I.M.; de Sebastián, J.; Poncela, A.V.; Lorenzana, A. Implementation of passive and active vibration control on an in-service footbridge. *Struct. Control Health Monit.* **2013**, *25*, e2208. [CrossRef]
24. Venuti, F.; Bruno, L. Mitigation of human-induced lateral vibrations on footbridges through walkway shaping. *Eng. Struct.* **2013**, *56*, 95–104. [CrossRef]
25. Jiménez-Alonso, F.J.; Sáez, A. Robust optimum design of tuned mass dampers to mitigate pedestrian-induced vibrations using multi-objective genetic algorithms. *Struct. Eng. Int.* **2017**, *27*, 492–501. [CrossRef]
26. Moutinho, C.; Cunha, Á.; Caetano, E.; de Carvalho, J.M. Vibration control of a slender footbridge using passive and semiactive tuned mass dampers. *Struct. Control Health Monit.* **2018**, *25*, e2208. [CrossRef]
27. Venuti, F.; Anna, R. Mitigation of human-induced vertical vibrations of footbridges through crowd flow control. *Struct. Control Health Monit.* **2018**, *25*, e2266. [CrossRef]
28. Qin, S.; Zhou, Y.-L.; Kang, J. Footbridge Serviceability Analysis: From System Identification to Tuned Mass Damper Implementation. *KSCE J. Civ. Eng.* **2019**, *23*, 754–762. [CrossRef]
29. Wang, D.; Wu, C.; Zhang, Y.; Li, S. Study on vertical vibration control of long-span steel footbridge with tuned mass dampers under pedestrian excitation. *J. Constr. Steel Res.* **2019**, *154*, 84–98. [CrossRef]
30. Soria, J.M.; Díaz, I.M.; García-Palacios, J.H. Further steps towards the tuning of inertial controllers for broadband-frequency-varying structures. *Struct. Control Health Monit.* **2020**, *27*, e2461. [CrossRef]
31. Gong, M.; Li, Y.; Shen, R.; Wei, X. Glass suspension footbridge: Human-induced vibration, serviceability evaluation, and vibration mitigation. *J. Bridge Eng.* **2021**, *26*, 05021014. [CrossRef]
32. Sétra. *Assessment of Vibrational Behaviour of Footbridges under Pedestrian Loading*; AFGC: Paris, France, 2006.
33. *ISO 10137*; Bases for Design of Structures—Serviceability of Buildings and Walkways against Vibrations. International Standard (ISO): Geneva, Switzerland, 2007.
34. HiVoSS. Design of Footbridges Guideline. Human Induced Vibrations of Steel Structures. 2008. Available online: http://www.stb.rwth-aachen.de/projekte/2007/HIVOSS/download.php(RFs2-CT-2007-00033) (accessed on 6 February 2021).
35. *NA to BS EN 1991-2-2003*; UK National Annex to Eurocode 1: Actions on Structures—Part 2: Traffic Loads on Bridges. British Standards Institution (BSI): London, UK, 2008.
36. Shrestha, B. Seismic response of long span cable-stayed bridge to near-fault vertical ground motions. *KSCE J. Civ. Eng.* **2015**, *19*, 180–187. [CrossRef]
37. Khanmohammadi, M.; Kharrazi, H. Residual Capacity of Mainshock-Damaged Precast-Bonded Prestressed Segmental Bridge Deck under Vertical Earthquake Ground Motions. *J. Bridge Eng.* **2018**, *23*, 04018016. [CrossRef]
38. Jin, Z.; Pei, S.; Li, X.; Liu, H.; Qiang, S. Effect of vertical ground motion on earthquake-induced derailment of railway vehicles over simply-supported bridges. *J. Sound Vib.* **2016**, *383*, 277–294. [CrossRef]
39. Paraskeva, T.S.; Dimitrakopoulos, E.G.; Zeng, Q. Dynamic vehicle–bridge interaction under simultaneous vertical earthquake excitation. *Bull. Earthq. Eng.* **2017**, *15*, 71–95. [CrossRef]
40. Xiang, Y.; Luo, Y.; Zhu, Z.; Shen, Z. Estimating the response of steel structures subjected to vertical seismic excitation: Idealized model and inelastic displacement ratio. *Eng. Struct.* **2017**, *148*, 225–238. [CrossRef]
41. Fayaz, J.; Zareian, F. Reliability Analysis of Steel SMRF and SCBF Structures Considering the Vertical Component of Near-Fault Ground Motions. *J. Struct. Eng.* **2019**, *33*, 04019046. [CrossRef]
42. Qu, Y.; Luo, Y.; Zhu, Z.; Huang, Q. An improved multidimensional modal pushover analysis procedure for seismic evaluation of latticed arch-type structures under lateral and vertical earthquakes. *Struct. Des. Tall Spec. Build.* **2019**, *28*, e1618. [CrossRef]
43. Rinaldin, G.; Fasan, M.; Noé, S.; Amadio, C. The influence of earthquake vertical component on the seismic response of masonry structures. *Eng. Struct.* **2019**, *185*, 184–193. [CrossRef]
44. Li, W.; Chen, Q. Effect of vertical ground motions and overburden depth on the seismic responses of large underground structures. *Eng. Struct.* **2020**, *205*, 110073. [CrossRef]
45. Chen, G.; Ruan, B.; Zhao, K.; Chen, W.; Zhuang, H.; Du, X.; Khoshnevisan, S.; Juang, C.H. Nonlinear Response Characteristics of Undersea Shield Tunnel Subjected to Strong Earthquake Motions. *J. Earthq. Eng.* **2020**, *24*, 351–380. [CrossRef]
46. Pourmasoud, M.M.; Lim, J.B.P.; Hajirasouliha, I.; McCrum, D. Multi-Directional Base Isolation System for Coupled Horizontal and Vertical Seismic Excitations. *J. Earthq. Eng.* **2020**, *26*, 1145–1170. [CrossRef]
47. Salehia, H.; Burgueñoa, R. Emerging artificial intelligence methods in structural engineering. *Eng. Struct.* **2018**, *171*, 170–189. [CrossRef]
48. Wang, X.; Mazumder, R.K.; Salarieh, B.; Salman, A.M.; Shafieezadeh, A.; Li, Y. Machine Learning for Risk and Resilience Assessment in Structural Engineering: Progress and Future Trends. *J. Struct. Eng.* **2022**, *148*, 03122003. [CrossRef]
49. Feng, D.-C.; Fu, B. Shear Strength of Internal Reinforced Concrete Beam-Column Joints: Intelligent Modeling Approach and Sensitivity Analysis. *Adv. Civ. Eng.* **2020**, *2020*, 8850417. [CrossRef]

50. Wang, X.; Li, Z.; Shafieezadeh, A. Seismic response prediction and variable importance analysis of extended pile-shaft-supported bridges against lateral spreading: Exploring optimized machine learning models. *Eng. Struct.* **2021**, *236*, 112142. [CrossRef]
51. Fu, B.; Feng, D.-C. A machine learning-based time-dependent shear strength model for corroded reinforced concrete beams. *J. Build. Eng.* **2021**, *36*, 102118. [CrossRef]
52. Fu, B.; Chen, S.-Z.; Liu, X.-R.; Feng, D.-C. A probabilistic bond strength model for corroded reinforced concrete based on weighted averaging of non-fine-tuned machine learning models. *Constr. Build. Mater.* **2022**, *318*, 125767. [CrossRef]
53. Safavian, S.R.; Landgrebe, D. A survey of decision tree classifier methodology. *IEEE Trans. Syst. Man Cybern.* **2002**, *21*, 660–674. [CrossRef]
54. Schalkoff, R.J. *Artificial Neural Networks*; McGraw-Hill: New York, NY, USA, 1997.
55. Zhou, Z.-H. Ensemble learning. In *Encyclopedia Biometrics*; Springer: Boston, MA, USA, 2015; pp. 411–416.
56. Feng, D.-C.; Liu, Z.-T.; Wang, X.-D.; Jiang, Z.-M.; Liang, S.-X. Failure mode classification and bearing capacity prediction for reinforced concrete columns based on ensemble machine learning algorithm. *Adv. Eng. Inform.* **2020**, *45*, 101126. [CrossRef]
57. Wei, X.; Russell, J.; Živanović, S.; Mottram, J.T. Measured dynamic properties for FRP footbridges and their critical comparison against structures made of conventional construction materials. *Compos. Struct.* **2019**, *223*, 110956. [CrossRef]
58. Oliveira, C.S. Fundamental Frequencies of Vibration of Footbridges in Portugal: From In Situ Measurements to Numerical Modelling. *Shock Vib.* **2014**, *2014*, 925437.
59. Ahmadi, E.; Caprani, C.C.; Heidarpour, A. An equivalent moving force model for consideration of human-structure interaction. *Appl. Math. Model.* **2017**, *51*, 526–545. [CrossRef]
60. Živanović, S.; Pavic, A.; Reynolds, P. Vibration serviceability of footbridges under human-induced excitation: A literature review. *J. Sound Vib.* **2005**, *279*, 1–74. [CrossRef]
61. Wei, X.; Liu, J.-C.; Bi, S. Uncertainty quantification and propagation of crowd behaviour effects on pedestrian-induced vibrations of footbridges. *Mech. Syst. Signal Process.* **2022**, *167 Pt A*, 108557. [CrossRef]
62. Wei, X. A simplified method to account for human-human interaction in the prediction of pedestrian-induced vibrations. *Struct. Control Health Monit.* **2021**, *28*, e2753. [CrossRef]
63. Fu, B.; Wei, X.; Chen, J.; Bi, S. Shear Lag Effects on Pedestrian-Induced Vibration and TMD-Based Vibration Control of Footbridges. *Struct. Eng. Int.* **2022**. [CrossRef]
64. Friswell, M.I.; Mottershead, J.E. *Finite Element Model Updating in Structural Dynamics*; Springer: Berlin/Heidelberg, Germany, 1995.
65. Clough, R.W.; Penzien, J. *Dynamics of Structures*, 3rd ed.; McGraw-Hill: New York, NY, USA, 2003.
66. Limongelli, M.; Siegert, D.; Merliot, E.; Waeytens, J.; Bourquin, F.; Vidal, R.; Le Corvec, V.; Gueguen, I.; Cottineau, L. Damage detection in a post tensioned concrete beam—Experimental investigation. *Eng. Struct.* **2016**, *128*, 15–25. [CrossRef]
67. Noble, D.; Nogal, M.; O'Connor, A.; Pakrashi, V. The effect of prestress force magnitude and eccentricity on the natural bending frequencies of uncracked prestressed concrete beams. *J. Sound Vib.* **2016**, *365*, 22–44. [CrossRef]
68. Bonopera, M.; Liao, W.-C.; Perceka, W. Experimental–theoretical investigation of the short-term vibration response of uncracked prestressed concrete members under long-age conditions. *Structures* **2022**, *35*, 260–273. [CrossRef]
69. Helbing, D.; Molnar, P. Social force model for pedestrian dynamics. *Phys. Rev. E* **1995**, *51*, 4282–4286. [CrossRef]
70. Chen, X.; Li, H.; Miao, J.; Jiang, S.; Jiang, X. A multiagent-based model for pedestrian simulation in subway stations. *Simul. Model. Pract. Theory* **2017**, *71*, 134–148. [CrossRef]
71. Helbing, D.; Farkas, I.; Vicsek, T. Simulating dynamical features of escape panic. *Nature* **2000**, *794*, 487–490. [CrossRef]
72. Li, M.; Zhao, Y.; He, L.; Chen, W.; Xu, X. The parameter calibration and optimization of social force model for the real-life 2013 Ya'an earthquake evacuation in China. *Saf. Sci.* **2015**, *79*, 243–253. [CrossRef]
73. Bachmann, H.; Ammann, W. *Vibration in Structures-Induced by Man and Machines*; International Association for Bridge and Structural Engineering (IABSE): Zurich, Switzerland, 1987.
74. Weidmann, U. *Transporttechnik der Fussgänger*; Ivt Report No. 90; ETH: Zurich, Switzerland, 1993.
75. Bruno, L.; Venuti, F. The pedestrian speed-density relation: Modeling and application. In Proceedings of the 3rd International Conference on the Design and Dynamic Behavior of Footbridges: Footbridge 2008, Porto, Portugal, 2–4 July 2008.
76. MOHURD (Ministry of Housing and Urban-Rural Development of the People's Republic of China). *Code for Seismic Design of Urban Bridges (CJJ 166-2011)*; China Architecture & Building Press: Beijing, China, 2011. (In Chinese)
77. Friedman, J.; Hastie, T.; Tibshirani, R. *The Elements of Statistical Learning*; Springer Series in Statistics: New York, NY, USA, 2001.